ACS APPLIED POLYMER MATERIALS

pubs.acs.org/acsapm
Article

Block Polyelectrolyte Additives That Modulate the Viscoelasticity and Enhance the Printability of Gelatin Inks at Physiological Temperatures

Tobias Göckler,[†] Fahed Albreiki,[†] Defu Li,[†] Alisa Grimm, Felix Mecklenburg, Juan Manuel Urueña, Ute Schepers, and Samanvaya Srivastava*

Cite This: *ACS Appl. Polym. Mater.* 2024, 6, 2427−2441

ABSTRACT: We demonstrate the utility of block polyelectrolyte (bPE) additives to enhance viscosity and resolve challenges with the three-dimensional (3D) printability of extrusion-based biopolymer inks. The addition of oppositely charged bPEs to solutions of photocurable gelatin methacryloyl (GelMA) results in complexation-driven self-assembly of the bPEs, leading to GelMA/bPE inks that are printable at physiological temperatures, representing stark improvements over GelMA inks that suffer from low viscosity at 37 °C, leading to low printability and poor structural stability. The hierarchical microstructure of the self-assemblies (either jammed micelles or 3D networks) formed by the oppositely charged bPEs, confirmed by small-angle X-ray scattering, is attributed to the enhancements in the shear strength and printability of the GelMA/bPE inks. Varying bPE concentration in the inks is shown to enable tunability of the rheological properties to meet the criteria of pre- and postextrusion flow characteristics for 3D printing, including prominent yielding behavior, strong shear thinning, and rapid recovery upon flow cessation. Moreover, the bPE self-assemblies also contribute to the robustness of the photo-cross-linked hydrogels; photo-cross-linked GelMA/bPE hydrogels are shown to exhibit higher shear strength than photo-cross-linked GelMA hydrogels. Last, the assessment of the printability of GelMA/bPE inks indicates excellent printing performance, including minimal swelling postextrusion, satisfactory retention of the filament shape upon deposition, and satisfactory shape fidelity of the various printed constructs. We envision this study to serve as a practical guide for the printing of bespoke extrusion inks where bPEs are used as scaffolds and viscosity enhancers that can be emulated in a range of photocurable precursors.

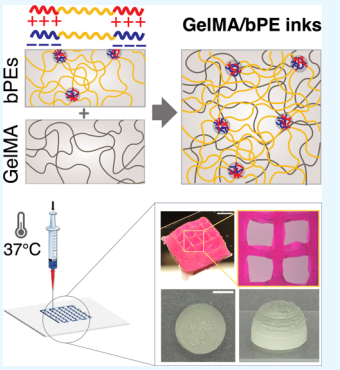

KEYWORDS: *biomaterials, 3D printing, biofabrication, polyelectrolyte complexation, hydrogels*

INTRODUCTION

Three-dimensional (3D)-printing technologies, i.e., the precise deposition of materials, such as metals, concrete, ceramics, polymers, or hydrogels, find applications in diverse disciplines, including architecture,[1,2] aerospace,[3,4] automotive,[5,6] electronics, consumer products,[7−9] and life sciences,[10−13] setting a benchmark for future manufacturing. In biomedical engineering, 3D-printing technologies have been utilized to create bioinspired, extracellular matrix-mimicking scaffolds that encapsulate living cells and feature tissue- or organ-like properties.[14−21] Among the various 3D-printing technologies, extrusion-based bioprinting (EBB) has enjoyed considerate attention for bioprinting owing to the ability to print structures with high cell loadings, low costs, fast manufacturing, and versatility.[22,23] However, the development of suitable inks that possess the optimal balance among printability, shape fidelity of printed structures, and biological response remains a significant bottleneck hindering the advancement of EBB technologies.[19,24−30]

Gelatin methacryloyl (GelMA) is one of the most popular and well-studied inks that find a satisfactory balance between shape fidelity and bioresponse.[31−33] Their broad commercial availability, simple chemical synthesis from gelatin, temperature-tunable viscoelastic properties, outstanding biocompatibility, surface adhesion characteristics for cells, and biodegradability encourage their widespread use as model inks in tissue engineering.[34−37] Yet, gelatin and other naturally derived polymers,[38] which are obtained by extraction from animal tissues, suffer from limited translation to biomedical contexts due to undesired flow properties of their solutions, including liquid-like behavior at 37 °C and weak response to stresses prior to secondary cross-linking as well as batch-to-batch

Received: May 22, 2023
Revised: January 2, 2024
Accepted: January 3, 2024
Published: February 21, 2024

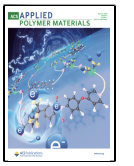

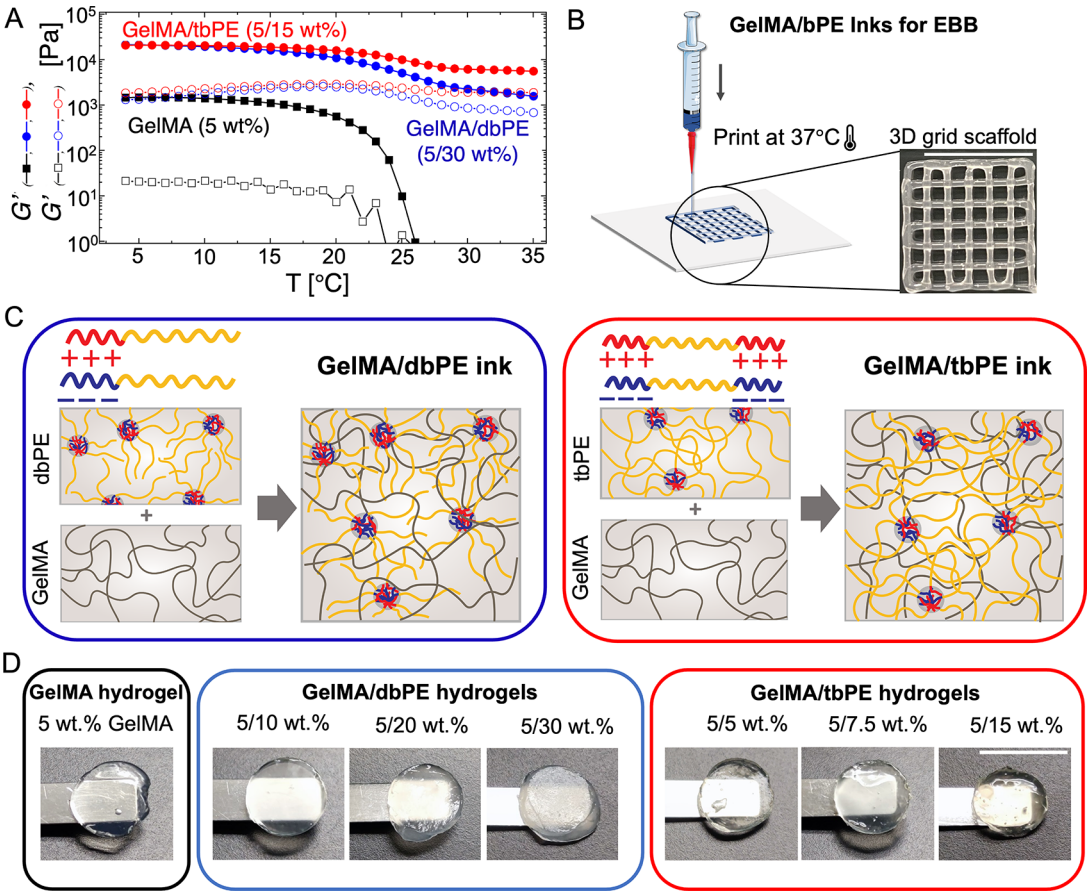

Figure 1. bPE-reinforced GelMA inks, which are 3D-printable at physiological temperatures. (A) Temperature evolution of the storage, G', and loss, G'', moduli of GelMA and GelMA/bPE inks demonstrating the gel−sol transition of GelMA inks, while GelMA/bPE inks sustain a high modulus upon heating to physiological temperatures. The moduli were measured with small amplitude oscillatory shear measurements at an angular frequency $\omega = 1$ rad·s^{-1} and strain $\gamma = 1\%$. (B) Representative example of extrusion printing of GelMA/dbPE inks onto a 12 × 12 mm grid structure. Scale bar = 1 cm. (C) Schematics representing the microstructure of GelMA/bPE inks comprising bPE self-assemblies with interspersed GelMA chains. Mixing oppositely charged dbPEs forms PEC micelles, while mixing tbPEs forms interconnected networks comprising neutral blocks bridging the PEC domains. (D) Series of photographs depicting hydrogel compositions obtained after photo-cross-linking GelMA and GelMA/bPE inks. Scale bar = 1 cm.

variability in the manufacturing process, leading to variation in the size, charge, and polydispersity of the polymer chains.[22,39] In comparison, synthetic polymers, especially poly(ethylene glycol) (PEG) derivatives such as PEG dimethacrylate, do not face such limitations because of their synthetic origin but typically lack biological functionality, suffer from intrinsic protein repellency, and exhibit low viscosities that are below the threshold of practical use in EBB, leading to undesirable flows and loss of form following deposition.[14,40,41]

The complementary benefits and shortcomings of gelatin and PEG-based inks have inspired attempts to combine them into one formulation. Such approaches aimed at utilizing the controlled biological activity of GelMA (such as cell adhesion and enzymatic degradability) with the controlled nontoxic mechanical reinforcements provided by PEG. PEG/GelMA hybrid hydrogels have been discussed extensively but have been limited to formulations where the gelatin and PEG building blocks were covalently co-cross-linked to each other.[42−45] As such, studies on systems wherein one of the networks is formed via physical interactions, providing an independent and mechanical platform and supporting cross-linking of the other network, are still lacking.

To address this biomaterials technology gap, we recently introduced versatile, biocompatible ink additives based on complex-forming block polyelectrolytes (bPEs), which enhance the printability of liquid-like inks.[46] Our recently reported strategy of using highly charged PEG-based macromolecules has been the first demonstration of harnessing spontaneous electrostatic self-assembly for modular ink design.[46,47] In our model inks, oppositely charged bPEs were employed as building blocks of electrostatic self-assemblies (micelles or interconnected networks)[48−51] and combined with GelMA, a representative low-viscosity ink lacking printability at 37 °C. Mixing the ink constituents resulted in hybrid GelMA/bPE inks with excellent 3D-printing performance. The bPE additives provided protective scaffoldings, preventing dilution in water[52] and a loss of structural integrity after deposition.[46] In addition, the hybrid GelMA/bPE hydrogels obtained after photo-cross-linking exhibited improved robustness due to the synergic effects of the entanglement of covalent and electrostatic networks.[46] Furthermore, in our previous work,[46] the biocompatibility of GelMA/bPE inks was investigated in two-dimensional (2D) and 3D toxicity studies using human hepatocarcinoma cell line HepG2 and calorimetric assay for assessing their metabolic

https://doi.org/10.1021/acsapm.3c01085
ACS Appl. Polym. Mater. 2024, 6, 2427−2441

activity (MTT). The cell viability was shown to depend on the bPE charge type, chemical structure, and their complexation state (complexation of bPE significantly increased the cell viability due to charge compensation). Live/dead fluorescent cell staining showed superior cell survival of GelMA/diblock polyelectrolyte (dbPE) compared to GelMA/triblock polyelectrolyte (tbPE) hydrogels. 3D-printed HepG2 cells using a suitable GelMA/dbPE formulation at 37 °C displayed a homogeneous cell distribution along horizontal and vertical axes because of immediate gelation of the ink inside the cartridge and cell adhesion on RGD sites within the gelatin backbone. Overall, electrostatic self-assembly was shown to be a viable method for suspending and printing cells without the need for additional cross-linking steps before printing.

In this study, we quantitatively assess the printability of GelMA/bPE inks at temperatures exceeding the typical melting point of gelatin and provide a parametric study of the mechanical properties of the hybrid inks that are relevant for extrusion-based printing. The self-assembled structures of bPE complexes are argued to ameliorate the mechanical properties of the GelMA-based inks. Variations in the bPE concentration, as well as the GelMA concentration and methacrylation level, revealed valuable insights into how the ink constituents influence the overall viscoelastic behavior. With the ink compositions that are shown to be optimal for printing, we further present quantitative assessments of ink printability in terms of preservation of the filament shape upon extrusion and deposition as well as the shape fidelity of 3D-printed structures. The analysis presented here provides a detailed understanding of the GelMA/bPE inks and fosters further applications in 3D printing and medical injections.

RESULTS AND DISCUSSION

GelMA/bPE Inks That Are Printable at Physiological Temperatures. GelMA solutions, synthesized from porcine skin gelatin sources (Figure S1), exhibit excellent printability at 22 °C, below their gelling temperature.[13,53] However, at 37 °C, GelMA solutions exhibit a low shear strength[54,55] and are *unprintable*. This transition is evident in Figure 1A, where GelMA inks (C_{GelMA} = 5 wt %) exhibited a well-known thermally induced decline in the shear moduli spanning over 3 orders of magnitude (depicted by black squares). The approximate crossover point between the storage and loss moduli (G' and G'', respectively) at T = 25 °C indicates a gel−sol transition. This behavior has been previously reported and attributed to the reversible disassembly of hydrogen-bonded triple helices of gelatin chains upon heating.[54]

Pairs of oppositely charged bPE additives imbued 37 °C printability to GelMA solutions by transforming them into self-assembled hydrogels. Previous work has shown that the complexation of oppositely charged bPEs, when restricted at the nanoscale, results in the formation of polyelectrolyte complex (PEC) hydrogels that feature tunability of the viscoelastic properties across a broad range and microstructural diversity.[48−50] We utilize these self-assembled hydrogels to provide the initial robustness to the inks, mitigating unwanted flows and enhancing the shape fidelity upon deposition prior to photo-cross-linking of GelMA chains (Figure 1B).

The oppositely charged bPEs we employed comprised poly(ethylene oxide) (PEO) and poly(allyl glycidyl ether) (PAGE) blocks, with the latter functionalized postsynthesis with ionizable groups (guanidinium chloride and sodium sulfonate) to create oppositely charged dbPEs or tbPEs. The synthesis and characterization of these bPEs are described in Schemes S1 and S2 and Figures S2 and S3. Figure 1C shows a schematic of the improved GelMA/bPE inks comprising uncross-linked GelMA mixed with oppositely charged dbPEs or tbPEs. PEC domains form swiftly upon mixing of the dbPE or tbPE pairs due to associative phase separation of the charged blocks.[49,50] At sufficiently high polymer concentrations, dbPEs form hydrogels comprising jammed micelles composed of PEC domains and surrounded by neutral PEO coronae (Figure 1C, left), while tbPEs form interconnected networks wherein a significant fraction of the neutral blocks bridge the PEC domains and a small fraction form loops (Figure 1C, right). In this work, these hydrogels will be referred to as dbPE and tbPE inks. In either case, the GelMA chains remain dispersed in the bPE inks, resulting in GelMA/bPE inks. We note that the dbPE and tbPE pairs were functionalized from the same PEO−PAGE and PAGE−PEO−PAGE block polymers, respectively, and mixed in charge-equivalent amounts. Therefore, charge mismatch between the oppositely charged bPEs was eliminated, resulting in strongly segregated PEC domains.

The moduli of the GelMA/bPE inks remained significantly higher than those of the corresponding GelMA inks at temperatures approaching 37 °C (Figure 1A). For $T \leq 25$ °C, the GelMA/bPE ink moduli were 1 order of magnitude higher than those of GelMA inks. Similar to GelMA inks, temperature-induced reductions in the moduli were observed for both GelMA/dbPE and GelMA/tbPE inks, which can again be attributed to the disruption of the hydrogen-bonded GelMA networks. However, the bPE self-assemblies provided sufficient shear strength ($\gtrsim 10^3$ Pa) to the hybrid inks at 37 °C. It can be surmised that the addition of complex-forming bPEs to GelMA can render inks that can be tuned for injection across a range of biologically relevant temperatures.

To demonstrate the extrusion-based printability of the GelMA/bPE inks, 12 × 12 mm grid structures were printed using GelMA/dbPE inks (Figure 1B). The structures were printed at 37 °C, which exceeds the melting temperature of gelatin solutions. In the absence of bPE additives, printing pure GelMA would have led to uncontrolled flows and a complete lack of shape fidelity (Figure S4). The grid shape illustrates the structural integrity and stability of the ink during the deposition of multiple layers at 37 °C, serving as a demonstration of overcoming the challenges involved in printing gelatin-based inks at physiological temperatures. Further assessment of the printability of the GelMA/bPE inks and demonstrations of the printed structures are discussed toward the end of this paper.

We also demonstrate that the addition of bPEs did not impede photo-cross-linking (photocuring) of the GelMA chains in a series of images in Figure 1D. The cured hydrogels remained transparent upon bPE addition, allowing for UV penetration and cross-linking among GelMA chains. The hydrogels, when cured in a cylindrical mold, retained their shape upon extraction from the mold and appeared to be similar to cured GelMA hydrogels. Direct evidence of the photo-cross-linking of GelMA chains within the bPE scaffolds was sought by monitoring the presence of methacrylate groups in the cross-linked hydrogels through NMR spectroscopy. GelMA chains in photo-cross-linked GelMA (5 wt %) and GelMA/tbPE (5/7.5 wt %) hydrogels, both prepared in D_2O, were incubated in excess D_2O containing 0.7 mg·mL^{-1} collagenase D type 2 and 5 mM $CaCl_2$ at 37 °C to enzymatically degrade cross-linked GelMA chains and dissolve

https://doi.org/10.1021/acsapm.3c01085
ACS Appl. Polym. Mater. 2024, 6, 2427−2441

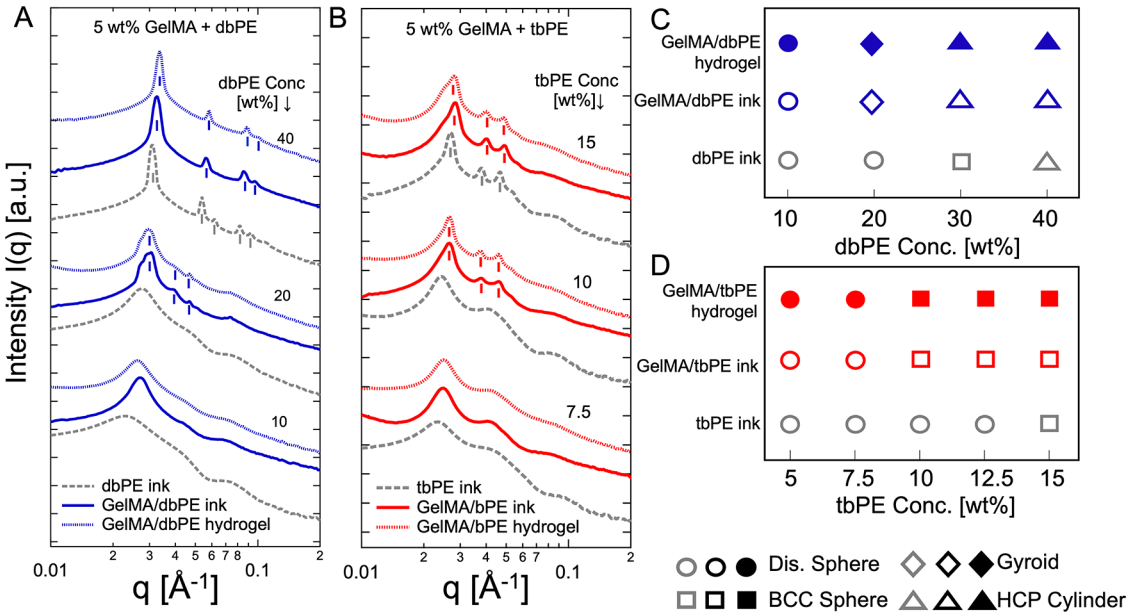

Figure 2. Diverse nanoscale morphologies of GelMA/bPE inks and hydrogels. SAXS intensity $I(q)$ versus wave vector q for GelMA/dbPE (A) and GelMA/tbPE (B) inks and hydrogels with varying bPE concentrations. Peak assignments for the ordered microstructures corresponding to the short vertical bars are provided in Tables S1−S7. Morphology maps of GelMA/dbPE (C) and GelMA/tbPE (D) inks and hydrogels with varying bPE concentrations (C_{GelMA} = 5 wt %).

the bPE scaffold. In the NMR spectra of the dissolved samples, the complete disappearance of methacrylate peaks that correspond to un-cross-linked GelMA samples was noted. A marked contrast between the NMR spectra (Figure S5) in the δ = 5.2−5.6 ppm region (where proton peaks of methacrylate groups are present) obtained from the un-cross-linked and cross-linked GelMA and GelMA/bPE inks and hydrogels strongly indicates nearly complete cross-linking of GelMA chains within the bPE scaffolds.

Furthermore, scanning electron micrographs (Figure S6) depicting the microstructure after photo-cross-linking reveal minimal differences between the GelMA and GelMA/bPE hydrogels. We note that rapid freezing of cross-linked GelMA and GelMA/bPE hydrogels can affect the porous microstructures of cross-linked GelMA chains and may not be the representative morphology in their hydrated state. Thus, this comparison of the micrographs serves only to indirectly portray similar GelMA mesh morphology in the GelMA and GelMA/bPE hydrogels.

GelMA/bPE Inks That Possess Hierarchical Microstructures. Contemporary hydrogels for tissue engineering applications need to possess mechanical properties commensurate with human tissues and pursue similarities with the tissue microstructures. Human tissues feature anisotropic hierarchal microstructures such as lamellar structure, which allows for directional biological functions aided by alignments of ordered bilayers.[56] However, the majority of traditional hydrogels (e.g., photo-cross-linked GelMA) possess isotropic micro- and macrostructures and have limited ability to achieve microstructure complexity commensurate to biological soft tissues.[43] Thus, GelMA hydrogels that feature tunable microstructures can further make them attractive materials to mimic human tissue structural complexity.

Small-angle X-ray scattering (SAXS) revealed the microstructure of GelMA/bPE inks, as depicted in Figure 2 (see also Figure S7). In the absence of bPEs, the spectra for GelMA solutions and cross-linked hydrogels resemble characteristic spectra for polymer solutions and cross-linked polymer networks, respectively (Figure S7). In the GelMA/bPE inks, the scattering from the PEC domains consisting of highly dense charged blocks of bPEs and high-atomic-number elements (e.g., sulfur and nitrogen) provide a stronger electron contrast than the surrounding environment and therefore dominate the scattering spectra.

Parts A and B of Figure 2 show a comparison of the one-dimensional (1D) intensity $I(q)$ versus wave vector q of the bPE inks (dashed lines), GelMA/bPE inks, and photo-cross-linked GelMA/bPE hydrogels (solid and dotted lines, respectively) with increasing concentrations of dbPEs (C_{dbPE}) and tbPEs (C_{tbPE}), respectively. The bPE inks (PEC hydrogels) featured a primary peak between q = 0.02 and 0.03 Å^{-1}, indicating the existence of PEC domains. These primary peaks persisted in both GelMA/dbPE (Figure 2A) and GelMA/tbPE (Figure 2B) inks and the respective photo-cross-linked GelMA/bPE hydrogels, with the peak positioning remaining largely invariant of the presence of GelMA chains in the inks or the interpenetrating network they form upon photo-cross-linking.

SAXS spectra with a broad primary peak without any secondary Bragg reflection peaks indicate a disordered arrangement of spherical PEC domains. Such spectra were noted for bPE inks with C_{dbPE} = 10 and 20 wt % (Figure 2A) or C_{tbPE} = 5, 7.5, 10, and 12.5 wt % (Figure 2B). At higher bPE concentrations, morphological transitions and ordering of the PEC domains were observed. For instance, the microstructure of the PEC domains evolved from disordered spheres to ordered spheres [with body-centered-cubic (BCC) arrangements] to hexagonal-close-packed (HCP) cylinders in dbPE inks upon increasing C_{dbPE} from 20 wt % to 30 wt % to 40 wt %, respectively (Figure 2C). These transitions were evident from the appearance of the sharp Bragg peaks, as can be noted for 40 wt % dbPE inks in Figure 2A, with the secondary peaks being located at $\sqrt{2}q^*$ and $\sqrt{3}q^*$ with respect to the location of the primary peak at q^*, corresponding to BCC arrangements

https://doi.org/10.1021/acsapm.3c01085
ACS Appl. Polym. Mater. 2024, 6, 2427−2441

of the PEC domains. Parts C and D of Figure 2 summarize the PEC domain morphology for dbPE and tbPE inks (gray symbols). Determinations of the microstructure by Bragg peak assignments are summarized in Tables S1−S7. A high degree of similarity between the measured and expected q/q^* values validates the assignments of the morphologies.

Transitions in the morphology of the PEC domains were also noted in response to the combination of GelMA with the bPEs. The presence of 5 wt % GelMA resulted in a transition of the PEC domains from disordered spheres to gyroid or from BCC spheres to HCP cylinders in GelMA/dbPE inks with C_{dbPE} = 20 and 30 wt %, respectively (Figure 2C). Similarly, a microstructural transition from disordered spheres to BCC spheres was observed in GelMA/tbPE inks with C_{tbPE} = 10 and 12.5 wt % (Figure 2D). In the range of bPE and GelMA concentrations investigated here, microstructural transitions were not noted upon photo-cross-linking GelMA/bPE inks; the structures were nearly identical before and after cross-linking (solid and dotted lines in Figure 2A,B).

The morphological transitions triggered by increasing C_{bPE} in GelMA/bPE inks and hydrogels were attributed to the macromolecular crowding induced by GelMA chains, reconfiguring the PEC domains. Similar transitions have been noted upon the incorporation of other cross-linkable polymers in bPE inks (PEC hydrogels).[52] We further posit that the macromolecular crowding induced by the GelMA chains also results in a lower extent of jamming among the PEC micelles formed by dbPEs (with decreased interdigitation among the micellar coronae) and partial reconfiguration of the PEC network formed by tbPEs (with a larger fraction of neutral midblocks forming loops compared to bridging between adjoining PEC domains), respectively. These reconfigurations would not be captured by the scattering spectra but are expected to manifest in the rheological response of the GelMA/bPE inks (discussed in the following sections). More importantly, these scattering investigations reveal that the presence of GelMA chains does not disrupt the self-assembly of the oppositely charged bPE chains. Moreover, compared to the amorphous structure of pure GelMA hydrogels, the incorporation of bPEs in the GelMA inks and hydrogels enriched its microstructural diversity, broadening the utility of GelMA in tissue engineering applications.

We note that all GelMA/bPE inks were prepared in Dulbecco's phosphate-buffered saline (DPBS), maintaining pH = 7.4, which lies within the isoelectric point (pI) of native gelatin type A ($7 < pI < 9$).[57] While gelatin and GelMA are both polyampholytes containing carboxylic acid and amino groups, the modification of gelatin into GelMA, pursued by methacrylation of the amino and hydroxyl groups on the gelatin backbone, shifts the pI to values approaching 4−5 and changes the availability of ionizable groups.[58,59] The pI and charge density of GelMA are, therefore, expected to depend on its degree of functionalization (DoF). Here, a particular concern is whether interactions between charged GelMA (above its pI) and bPEs lead to the complexation of GelMA with bPE and/or whether GelMA influences the complexation-driven self-assembly of the oppositely charged bPEs, leading to an inhomogeneous microstructure (flocculation and phase separation) within the GelMA/bPE inks. The SAXS spectra were collected for GelMA/bPE inks (comprising high-DoF GelMA) at multiple spots in each sample; the similarity of the scattering spectra obtained from multiple spots indicates the absence of heterogeneity in the sample's microstructure and/or flocculation or macrophase separation. Moreover, the invariant primary peak position in the SAXS spectra in the presence of GelMA in the inks and the photo-cross-linked hydrogels all point toward the minimal influence of GelMA on the self-assembly of bPEs. Additionally, we showed in our previous study[52] that the microstructural evolutions of the GelMA-based inks and hydrogels are similar to those of the corresponding systems wherein PEG diacrylate (PEGDA) was employed as the cross-linkable polymer, indicating that GelMA and PEGDA play similar roles as "inert crowders" in the PEC hydrogels. Therefore, we believe that GelMA does not substantially influence the bPE self-assembly, which is attributable to the low density of the ionized groups on the high-DoF GelMA chains.

Moreover, the scattering investigations also enable us to posit that GelMA chains are dispersed within the PEC network, occupying space between the PEC domains/cores. Therefore, we do not expect any microphase separation or the formation of microcrystalline grains of the PEC domains. We elaborate on our hypothesis as follows: Because the hydrodynamic radius of gelatin is on the order of 19−27 nm[60] and considering that the distance between PEC domains (or interdomain distances) is estimated to range from 22 to 27 nm, we expect that GelMA chains are similar or smaller in size compared to the interdomain distances, and there is no obvious reason to expect their expulsion. Additionally, the order of ink preparation is crucial for ensuring homogeneity and good dispersion of GelMA within PEC assemblies. GelMA precursors were first mixed with sulfonate-functionalized bPEs to form homogeneous solutions, and guanidinium-functionalized bPEs were then added to the solutions, in which oppositely charged polyelectrolytes rapidly formed PEC networks with the presence of GelMA precursors. Nearly identical SAXS spectra were obtained from multiple locations of the samples, providing further confirmation of the homogeneity of the inks and their interpenetrating networks upon UV irradiation. Moreover, the peak positions in the SAXS spectra did not shift significantly when GelMA chains were introduced in the PEC inks (to form GelMA/bPE inks) or upon their cross-linking to form GelMA/bPE hydrogels. The PEC domains would have been expected to be pushed closer to each other if microcrystalline grains of the PEC domains had formed. Last, the mechanical property enhancements (as demonstrated in a later section) that we achieve in the photo-cross-linked GelMA/bPE hydrogels would not have emerged if grain formation had occurred because it would have resulted in poorer mechanical properties emerging from a poorly connected GelMA network.

Tunable Linear Viscoelastic (LVE) Response of GelMA/bPE Inks. Bulk rheological investigations enable facile assessment of the printability and the mechanical integrity of inks prior to and after printing as well as after cross-linking.[27,61] The representative response of bPE inks at 37 °C with and without GelMA to oscillatory strain within the LVE regime is presented in Figures S8 and S9. The storage and loss moduli (G' and G'') of dbPE inks (C_{dbPE} = 20 wt %) were noted to be similar across the range of ω investigated here. A 1 order of magnitude reduction in both moduli was noted upon the addition of 5 wt % GelMA to the dbPE inks. In contrast, tbPE inks (Figures S8 and S9) exhibited only a minor reduction in the overall magnitude of the LVE response when GelMA was added.

https://doi.org/10.1021/acsapm.3c01085
ACS Appl. Polym. Mater. 2024, 6, 2427−2441

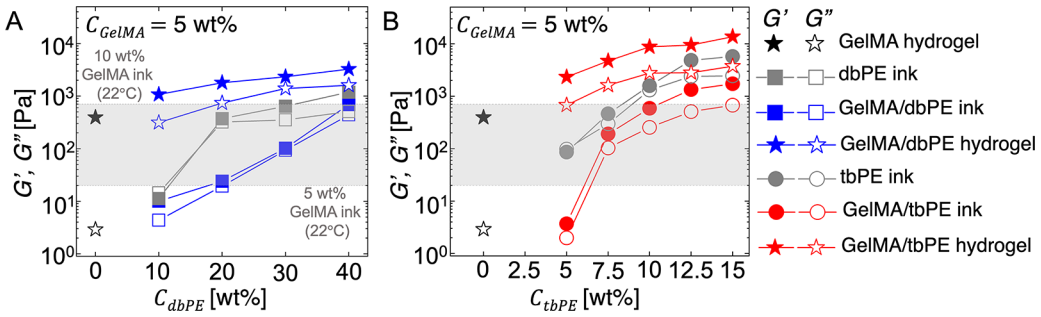

Figure 3. GelMA/bPE inks and hydrogel moduli tuned by varying the bPE concentrations. Storage (G') and loss (G'') moduli for GelMA/dbPE (A) and GelMA/tbPE (B) inks and hydrogels with varying bPE concentrations C_{bPE} (C_{GelMA} = 5 wt %). The moduli were measured with oscillatory shear measurements at angular frequency = 1 rad·s^{-1} and strain = 1% at 37 °C. The shaded region highlights the window of fabrication, corresponding to G' of GelMA inks (5−10 wt % at 22 °C).[46]

The evolution of the shear moduli of GelMA/dbPE inks as a function of C_{dbPE} is shown in Figure 3A. The moduli of GelMA/dbPE inks were generally lower than those of the corresponding dbPE inks (compared data sets depicted by squares and circles). The moduli of dbPE inks increased rapidly from C_{dbPE} = 10 to 20 wt % and then plateaued for ∼10^3 Pa at $C_{dbPE} \geq$ 20 wt %. In contrast, both G' and G'' increased almost linearly with increasing C_{dbPE} in GelMA/dbPE inks. A smaller impact of GelMA inclusion on the GelMA/dbPE ink moduli was noted at low C_{dbPE} and could be ascribed to low interdigitation of the micellar coronae. In contrast, at higher C_{dbPE} = 40 wt %, significant interdigitation of micellar coronae can accommodate the GelMA chains without the moduli decreasing markedly.

The effect of GelMA on the moduli of tbPE inks, in contrast, was most pronounced at the lowest tbPE concentrations, C_{tbPE} = 5 wt %, wherein G' and G'' reduced by ∼1.5 orders of magnitude (Figure 3B). For $C_{tbPE} \geq$ 7.5 wt %, while the shear moduli of GelMA/tbPE inks tended to be lower than the moduli of the tbPE inks, they could be considered proximal to each other. With increasing C_{tbPE}, the extent of segregation of the PEC domains is expected to diminish due to a higher fraction of bridging PEO midblocks, even in the presence of GelMA chains, resulting in the sustenance of the moduli.

Photo-cross-linking GelMA in the GelMA/bPE inks using ultraviolet (UV) irradiation led to a notable enhancement in the shear moduli. The formation of interlaced water-laden PEC and GelMA networks resulted in GelMA/bPE hydrogels with robust shear moduli. The moduli values of the hydrogels in their cross-linked states were more pronounced at low concentrations, where 2−3 orders of magnitude increases in G' in both GelMA/bPE hydrogels (comparing circles with stars) were noted (Figure 3A,B; see also Figure S10). At higher C_{bPE}, the shear moduli of the hydrogels exhibited enhancements of nearly 1 order of magnitude compared to their moduli in their ink states.

GelMA/bPE Inks That Exhibit Tunable Yielding and Shear-Thinning Characteristics. Well-defined yield stress behavior is a requirement for bioinks to allow a stable suspension of cells in ink at rest in a syringe, while a flow initiation point can be achieved upon applying sufficient stress. This is also an important consideration because it determines the required pressure for pneumatic extrusion.[62] We quantify the yield stress behavior (the stress required for the materials to flow or yielding transition, $\sigma \gtrsim \sigma_y$) at 37 °C to further establish the suitability of GelMA/bPE formulations as 3D-printing inks. Figure 4A depicts a comparison of the viscosity,

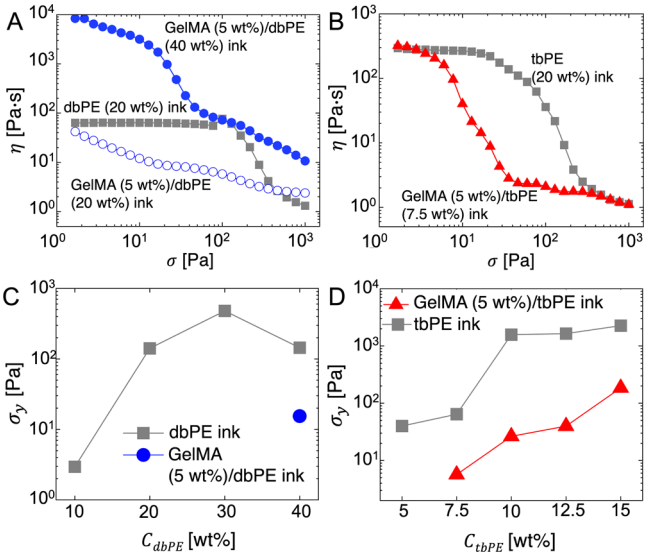

Figure 4. Yielding behavior of GelMA/bPE hybrid inks. Shear viscosity, η, as a function of shear stress, σ, for (A) dbPE (C_{dbPE} = 20 wt %) and GelMA/dbPE (C_{dbPE} = 20 and 40 wt %; C_{GelMA} = 5 wt %) inks and (B) tbPE (C_{tbPE} = 7.5 wt %) and GelMA/tbPE (C_{tbPE} = 7.5 wt %; C_{GelMA} = 5 wt %) inks. Yield stress, σ_y, as a function of the bPE concentration for (C) dbPE and GelMA/dbPE and (D) tbPE and GelMA/tbPE inks.

$\eta = \sigma/\dot{\gamma}$, as a function of the shear stress, σ, for dbPE inks with C_{dbPE} = 20 wt % and GelMA/dbPE inks with C_{dbPE} = 20 and 40 wt % and C_{GelMA} = 5 wt % (see also Figure S11). In these flow curves, the stress corresponding to the crossover point of η from the solid ($\sigma < \sigma_y$ with $\eta \sim$ constant) to the fluid ($\sigma > \sigma_y$, where $\sigma = \sigma_y + \dot{\gamma}^n$) regime was designated as the yield stress σ_y.[63] dbPE inks of 20 wt % exhibited a yield point at σ_y = 100 Pa, while no apparent yield point was identifiable for the corresponding GelMA/dbPE inks. Increasing C_{dbPE} up to 40 wt %, however, resulted in GelMA/dbPE inks with a well-defined yield point (σ_y = 15.4 Pa). The measurable σ_y values as a function of C_{dbPE} for dbPE inks without or with GelMA are summarized in Figure 4C. dbPE inks behaved as yield stress fluids and demonstrated distinct σ_y values across all C_{dbPE}, where σ_y increased with C_{dbPE} until 30 wt % and then decreased for C_{dbPE} = 40 wt %. The latter could be attributed to the morphological transition of the PEC domains from BCC spheres to HCP cylinders. The presence of GelMA obscured the yielding behavior in dbPE inks, except at relatively high C_{dbPE} = 40 wt %, where a measurable σ_y value was noted,

https://doi.org/10.1021/acsapm.3c01085
ACS Appl. Polym. Mater. 2024, 6, 2427−2441

although nearly 1 order of magnitude lower than σ_y for the corresponding dbPE inks. These observations correlate well with the reduction of the shear moduli upon the combination of GelMA and dbPEs in GelMA/dbPE inks (Figure 3A,C) and can again be attributed to the disrupting effect of GelMA chains on the interdigitation of the micellar coronae and diminished extent of jamming until at sufficiently high C_{dbPE}, wherein the micellar coronae remained adequately interdigitated even in the presence of GelMA chains, enabling stress buildup until yielding.

In contrast, the presence of GelMA did not eliminate the yielding behavior in tbPE inks (Figure 4B). However, σ_y reduced upon the combination of GelMA with the tbPEs (for instance, from σ_y = 70 to 7 Pa for C_{tbPE} = 7.5 wt % and C_{GelMA} = 5 wt %), indicating that the solid regime of the material was sustained only until smaller imposed stresses. Figure 4D depicts the measurable yield stresses σ_y as a function of C_{tbPE} for tbPE and GelMA/tbPE inks. tbPE inks exhibited a yielding transition across a wide range of C_{tbPE} values regardless of GelMA inclusion (except at the lowest C_{tbPE} = 5 wt %). The yield stress values, σ_y, however, were consistently lower for GelMA/tbPE inks than for the corresponding tbPE inks across all C_{tbPE} values, attributable to a lower fraction of bridging midblocks between the PEC domains in the presence of GelMA and consistent with the observations of lower moduli of GelMA/tbPE inks compared to tbPE inks (Figure 3B,D). At the same time, a monotonic increase of σ_y as a function of C_{tbPE} in both formulations is attributed to the increase in the PEC network density. We note that yielding in tbPE inks is posited to occur through chain pullout (and the eventual rupture of PEC domains at high enough shear rates). Similar yielding behavior has been demonstrated in tbPE PEC hydrogels (comprising only the oppositely charged tbPE chains) by us[49] as well as others.[64,65] As noted by Kim et al.,[65] the chain pullout times can be modulated by adjusting the charged block length, polymer volume fraction, strength of the electrostatic association, and temperature. Overall, these observations of yielding behavior are relevant in cases when the injectability and extrudability of (bio)inks need to be precisely controlled for certain injection parameters (e.g., needle radius and length) and process parameters (injection pressure and flow rate).[62] Moreover, we tested the creep compliance by monitoring the strain at a fixed stress for representative ink formulations (5/7.5 wt % GelMA/tbPE inks) to further establish the validity of the yielding behavior. The inks exhibited solid-like behavior below their yield stress $\sigma < \sigma_y$, and the compliance was nearly steady beyond the instantaneous elastic response. In contrast, when the stress imposed on the ink was above the yield stress $\sigma > \sigma_y$, the measured compliance was significantly higher and continued to rise during the measurement time (300 s), indicating that the sample deforms at high stresses (Figure S12).

A prominent shear-thinning response was also noted for the GelMA/bPE inks (Figure 5; see also Figure S13). Quantifying the shear-thinning behavior is of importance in determining the velocity of (bio)ink extrusion through a small needle and the associated time scales for material collection during deposition. Here, shear thinning was observed as a decrease in the complex shear viscosity, η^*, as a function of the angular frequency, ω, from small-amplitude oscillatory shear experiments. For 20 wt % dbPE inks, we observed a Newtonian response (constant η^* for $\omega < 0.2$ rad·s^{-1}) followed by a shear-thinning response for $\omega > 0.2$ rad·s^{-1} (gray squares in Figure 5A). Similar behavior was also observed for 7.5 wt % tbPE inks (Figure 5B). The shear-thinning response was quantified using the Carreau−Yasuda model, which suggests the ω dependence of η^* as

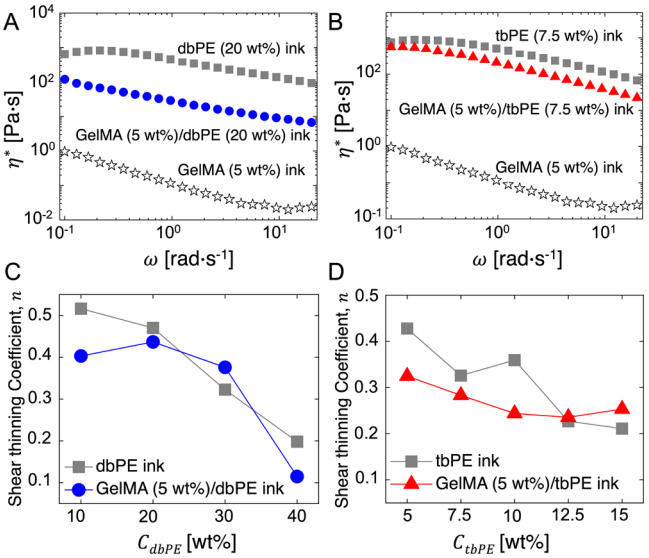

Figure 5. Shear-thinning behavior of GelMA/bPE inks. Complex shear viscosity, η^*, as a function of the angular frequency, ω, for (A) GelMA (C_{GelMA} = 5 wt %), dbPE (C_{dbPE} = 20 wt %), and GelMA/dbPE (C_{GelMA} = 5 wt %; C_{dbPE} = 20 wt %) inks and (B) GelMA (C_{GelMA} = 5 wt %), tbPE (C_{tbPE} = 7.5 wt %), and GelMA/tbPE (C_{GelMA} = 5 wt %; C_{tbPE} = 7.5 wt %) inks. Shear-thinning coefficients, n, as a function of the bPE concentration for (C) dbPE and GelMA/dbPE and (D) tbPE and GelMA/tbPE inks.

$$\eta^*(\omega) = \eta_0^*[1 + (\lambda\omega)^a]^{n-1/a} \quad (1)$$

with η_0^* being the zero-shear complex viscosity, λ being the relaxation time, n being the shear-thinning exponent (power law index), and a describing the width of the transition from a Newtonian shear-independent fluid to a power law fluid.[66]

GelMA/bPE inks also exhibited shear-thinning behaviors (Figure 5A,B), albeit with lower η^* and, in some cases, an inaccessible Newtonian flow regime (Figure 5A). The shear-thinning behaviors in such cases were described as a power law with a consistency index K as

$$\eta^*(\omega) = K\omega^{n-1} \quad (2)$$

The shear-thinning exponents n for the dbPE and GelMA/dbPE inks are summarized in Figure 5C. A decrease in n, corresponding to stronger shear thinning, was noted with increasing C_{dbPE} for the dbPE inks. In contrast, n remained nearly constant until $C_{dbPE} \leq 30$ wt % and then sharply decreased at C_{dbPE} = 40 wt % for GelMA/dbPE inks. This is consistent with the yielding behavior of the GelMA/dbPE inks, wherein up to concentrations $C_{dbPE} \leq 30$ wt %, no yielding was observed due to diminished jamming among the micelles and, correspondingly, weak shear thinning was observed as micelles rearranged readily in response to the applied stress, while at C_{dbPE} = 40 wt %, the micellar coronae are sufficiently jammed, leading to a yielding behavior and strong shear thinning once yielding has occurred.

GelMA/tbPE inks also exhibited shear-thinning behavior consistent with their yielding behavior. Specifically, a lower fraction of bridging midblocks between the PEC domains in

https://doi.org/10.1021/acsapm.3c01085
ACS Appl. Polym. Mater. 2024, 6, 2427−2441

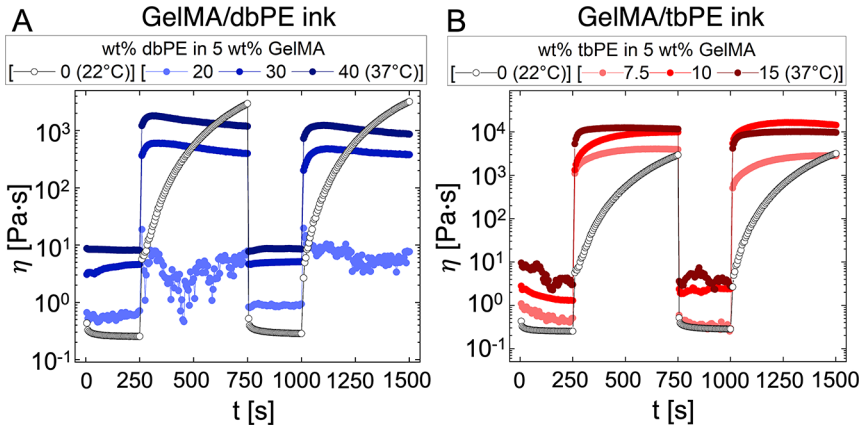

Figure 6. Rapid viscoelastic recovery of GelMA/bPE inks. Swift viscosity recovery after deformation at high shear rates is observed for (A) GelMA/dbPE and (B) GelMA/tbPE inks at 37 °C. In contrast, GelMA inks recover significantly slowly after shearing at 22 °C. Recovery tests were conducted by applying two sequential steps with a fixed shear rate $\dot{\gamma}$ = 100 s^{-1} for 250 s, followed by a lower shear rate $\dot{\gamma}$ = 0.01 s^{-1} for 500 s.

the presence of GelMA resulted in stronger shear-thinning behaviors compared to those of tbPE inks (Figure 5B,D). Previously reported models to assess the extrusion velocity use the shear-thinning exponent as a key parameter. Control over the shear-thinning behavior, as exemplified here for the GelMA/bPE inks, provides opportunities for tuning and expanding the injectability window of these inks, in which printability can be accessed over a range of velocities and collection speeds.[62,67]

Additional quantification of the shear-thinning response of GelMA/bPE inks using rotational shear rheology measurements was conducted to establish a comparison between oscillatory and rotational shear measurements. The similarity between the shear rate dependence and frequency dependence of shear flow is empirically described using the Cox−Merz rule.[68] The applicability of the Cox−Merz rule is limited for our materials, as shown in Figure S14. The breakdown of the Cox−Merz relationship is an expected result for PEC hydrogels; this breakdown is a well-known result in physically associating polymer solutions.[69] In such systems, the viscosity (and the high-frequency elastic modulus) depends on the number of "elastically effective chains" in which the disengagements between the associations (in our case, the complexed PEC domains) and their rate determine the overall topology of the network under various deformations.[69] Because rotational and oscillatory deformations can impose very different strain fields on the material, they probe the disengagements at different lengths and time scales. As such, the number density of elastically effective chains is different in each deformation, producing different rate-dependent shear-thinning behaviors.

Rapid Viscoelastic Recovery of GelMA/bPE Inks. After extrusion through a small nozzle, the recovery of inks (transition from liquid-like to solid-like flow behavior) dictates the resolution of printing, the shape fidelity, and the construction of precise multilayered structures.[61] Figure 6 contrasts the shear viscosity recovery of GelMA/bPE inks at 37 °C with the recovery of GelMA inks at 22 °C. The time-dependent viscosity η was measured during the sequential application of a high shear rate ($\dot{\gamma}$ = 100 s^{-1}) for 250 s, followed by a low shear rate ($\dot{\gamma}$ = 0.01 s^{-1}) for 500 s. GelMA inks (22 °C) required long times (≥8 min) for viscosity recovery, which is attributable to the slow recovery of the hydrogen-bonded triple-helix structure of gelatin chains. In contrast, GelMA/bPE inks (37 °C) exhibited very fast viscosity recovery.

Inks containing dbPEs exhibited near-complete recovery with C_{dbPE}-independent recovery time scales, as is evident in Figure 6A. A minor decay of the low $\dot{\gamma}$ viscosity was noted for inks with $C_{dbPE} \geq 30$ wt %, indicating slow structural rearrangements of the jammed PEC micelles. At the same time, inks containing lower concentrations of dbPEs (C_{dbPE} = 20 wt %) exhibited a low η but complete recovery associated with the fast structural rearrangements of the partially jammed PEC micelles.

The recovery of GelMA/tbPE inks, especially at $C_{tbPE} \leq 10$ wt %, comprised a prominent, near-instant first step, followed by a subtle, slow second step (Figure 6B). The slow second step also showed a weak C_{tbPE} dependence, becoming faster with increasing C_{tbPE}. We attribute this behavior to larger disruption and reconfiguration of the weaker PEC network at low C_{tbPE} due to the low network density. This disruption can also explain the incomplete recovery at low C_{tbPE} transitioning to near-complete recovery at high C_{tbPE} (Figure 6B). At the same time, the increasing robustness and connectivity of the PEC network led to its larger disruption in the high-$\dot{\gamma}$ regime, resulting in an appreciable thixotropic decrease in η during the first shearing cycle of the high C_{tbPE} inks (Figure 6B). We note that thixotropy is a time-dependent decline in viscosity in response to shear stress at a fixed shear rate and is distinguishable from the shear-thinning behavior wherein the viscosity depends on $\dot{\gamma}$ but is independent of time.[70]

Moduli of GelMA/bPE Inks and Hydrogels That Can Be Tuned by Varying the Photo-Cross-Linking Density. GelMA-based inks (including the GelMA/bPE inks) are photocurable, demonstrating appropriate stiffness for tissue engineering applications.[43,44,55] We further investigated the effects of the GelMA photo-cross-linking density, modulated by either its concentration or its methacrylation levels (also referred to as the DoF), on the viscoelastic properties of GelMA/bPE inks before and after photo-cross-linking. Increasing C_{GelMA} corresponds to a larger number density of GelMA chains and the photo-cross-linkable methacrylate groups, whereas increasing DoF corresponds to inks with the same concentration of GelMA chains but with a higher number density of methacrylate groups per GelMA chain.

Generally, the shear moduli were reduced upon increasing C_{GelMA} in GelMA/bPE inks (Figure 7A,B; see also Figures S15

https://doi.org/10.1021/acsapm.3c01085
ACS Appl. Polym. Mater. 2024, 6, 2427−2441

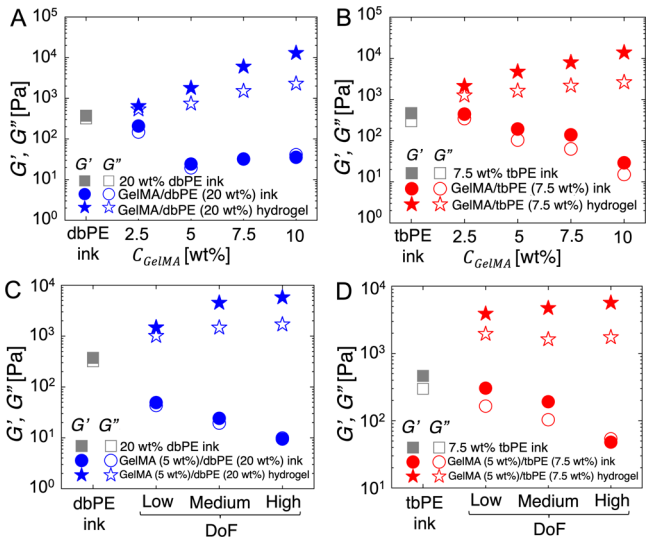

Figure 7. Tunability of the ink and hydrogel shear moduli with varying photo-cross-linking density. Storage (G') and loss (G'') moduli of (A) GelMA/dbPE inks and hydrogels and (B) GelMA/tbPE inks and hydrogels as a function of the GelMA concentration. Dependence of G' and G'' of (C) GelMA/dbPE inks and hydrogels and (D) GelMA/tbPE inks and hydrogels on the degree of methacrylate group functionalization or DoF of the GelMA chains. The moduli were measured with small-amplitude oscillatory shear measurements at angular frequency = 1 rad·s^{-1} and strain = 1% at 37 °C.

and S16). The moduli of GelMA/dbPE inks decreased by nearly 2 orders of magnitude upon increasing C_{GelMA} from 0 to 5 wt %, beyond which they remained nearly constant (Figure 7A). In contrast, the moduli of GelMA/tbPE inks weakened monotonically with increasing C_{GelMA}. Consistent with earlier observations, these decays in the shear moduli upon increasing GelMA content can be attributed to an increasing reduction of the coronal interdigitations and disruption of the PEC network in the dbPE and tbPE inks by the GelMA chains.

Photo-cross-linking GelMA chains in the GelMA/bPE inks led to an opposite trend in moduli evolution. A monotonic increase in the shear moduli, spanning more than 1 order of magnitude, was noted in both GelMA/dbPE and GelMA/tbPE hydrogels with increasing C_{GelMA} (Figure 7A,B, star symbols). Elastic moduli were appreciably higher than loss moduli, especially at higher C_{GelMA}. These moduli enhancements were expected to emerge from the higher cross-linking density in the GelMA network and can serve as a guide for tuning the strength of GelMA hydrogels for various tissue engineering purposes.[36]

The level of methacrylate groups, or DoF, along the GelMA chain can be conveniently tuned by controlling the amine substitution with varying amounts of methacrylic anhydride.[54] Previously, higher DoF has been shown to hinder the formation of triple helices between gelatin chains at low temperatures, leading to weaker gels prior to cross-linking.[54] This weakening has been attributed to the hindering of the triple helices formation by the vinyl side groups.[54] The trends of the GelMA/bPE ink moduli with increasing GelMA DoF are shown in Figure 7C,D and are noted to mirror the trends produced upon increasing C_{GelMA}. Increasing the density of the vinyl side groups in GelMA led to an observable decrease in G' and G'' due to the increasing hydrophobicity of the GelMA chains, resulting in a larger steric hindrance of the PEC network.[47] At the same time, photo-cross-linking the three GelMA/bPE inks with increasing DoF resulted in progressively increasing stiffness due to denser covalent networks and larger interpenetration among the covalent and electrostatic micelles/networks (Figure 7C,D; see also Figures S17 and S18). Moreover, the increased cross-linking density of the GelMA network could increase jamming among the dbPE micelles by restricting their translational relaxation and creating additional entanglements with the tbPE networks, resulting in higher hydrogel moduli.

Printability Assessments of GelMA/bPE Inks. To demonstrate the 3D printability of GelMA/bPE inks, several structures were printed using two different printers mentioned in the Materials and Methods section. The structures were analyzed to meet the requirements for high-fidelity printing. For extrusion-based printing, inks are typically loaded into disposable syringes and dispensed either pneumatically or mechanically.[23] In both cases, the printability can be quantified using property−function relationships in which the ink extrusion rate Q (feed rate), the printhead or translational speed V, and the pressure P required to initiate the flow (for pneumatic air pump printers) are primary control parameters.

First, we demonstrated the printability of a representative GelMA/tbPE ink (5/15 wt %) due to its sufficiently high shear moduli and prominent shear-thinning properties, well-defined yield stress behavior, and rapid structural recovery. GelMA/tbPE ink filaments extruded at different rates ranging from 1 to 10 μL·s^{-1} were noted to extrude uniformly (Figure 8A). The filament diameter and swelling ratio (the ratio of the as-extruded filament to the nozzle diameter) remained nearly invariant of the extrusion rates Q (Figure 8B), indicating reliable extrusion of the GelMA/tbPE inks and minimal postextrusion swelling.

To assess the fidelity of the printed filaments and ascertain their spreading upon deposition, which can both be critical for the printing of intricate constructs, filament fusion tests were carried out, as shown in Figure 8C. GelMA/tbPE ink filaments were printed in patterns with decreasing interfilament distances that approach the nozzle size at the smallest scales. The diameter D of the deposited filaments was measured by imaging the filaments. At a constant translational speed of V = 1 mm·s^{-1}, the printability characteristics (estimated using the spreading ratio or the ratio of the deposited filament to the inner nozzle diameter[71]) were found to be strongly dependent on the extrusion rate Q (Figure 8D). The lowest Q = 0.01 μL·s^{-1} resulted in the highest resolution of printing (or the lowest spreading ratio), emerging from the least accumulation of ink on the substrate. With increasing Q, the printing resolution worsened because excessive deposition of the inks resulted in filament spreading (Figure 8D) and subsequent fusion of the filaments when the gap between the filaments became insufficient (indicated by the dashed rectangles in Figure 8C).

The diameter of a nonspreading deposited filament of a circular cross section can be predicted using simple volume conservation as $D = (2/\sqrt{\pi})(Q/V)^{1/2}$. This dependence of the deposited filament diameter D on the extrusion parameters Q/V at a fixed distance between the nozzle tip and surface h is depicted by the dashed line in Figure 8E. For the GelMA/tbPE ink filaments, in agreement with the low spreading noted at low Q (Figure 8D), D was close to the predicted values, especially in the low Q/V region (Figure 8E). At high Q/V, the spreading of the filaments led to deviations from the expected behavior, with the spreading of the deposited filaments

https://doi.org/10.1021/acsapm.3c01085
ACS Appl. Polym. Mater. 2024, 6, 2427−2441

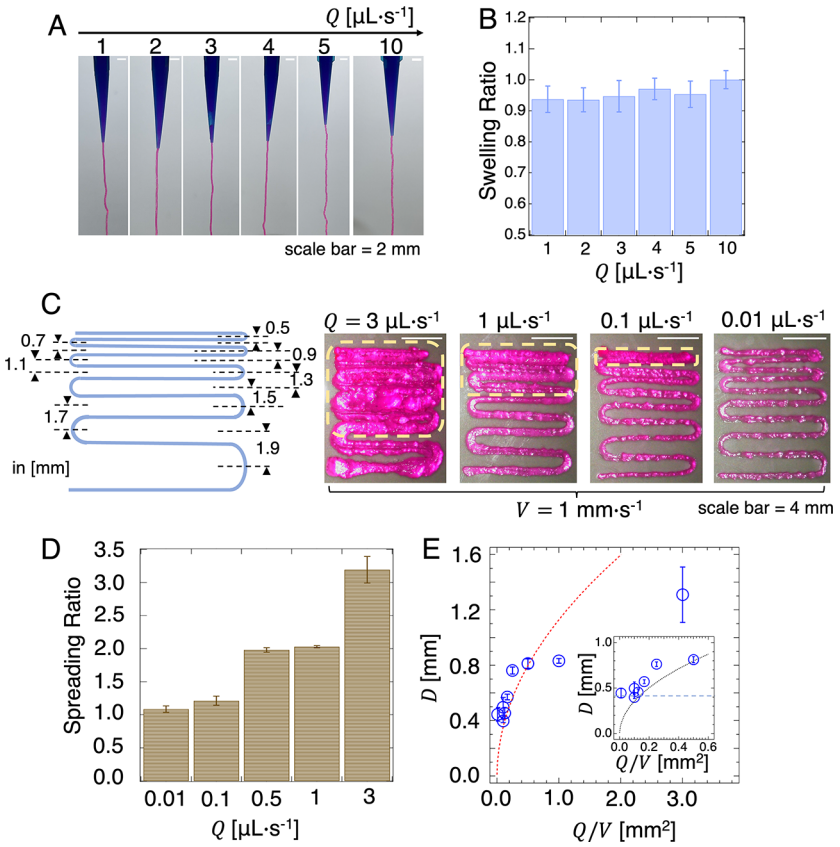

Figure 8. Printability assessment of GelMA/bPE inks. (A) As-extruded filaments using GelMA/tbPE ink (5/15 wt %) and (B) their swelling ratio characteristics at various extrusion rates. (C) Filament fusion test including a schematic diagram of the printing patterns with decreasing interfilament distances and optical microscopy snapshots showing tunable porous characteristics at different extrusion rates and a constant printhead velocity. (D) Filament spreading ratio characteristics from the fusion test showing the dependence of the filament size on the extrusion parameters. (E) Filament diameter D dependence on the extrusion parameters Q and V at a fixed distance h between the nozzle tip and print bed. Open symbols represent GelMA/bPE ink filaments. The black dashed line is the predicted diameter from volume conservation assuming a circular line. Inset: Dependence at the Q/V region, where the horizontal blue dashed line indicates the inner diameter of the nozzle tip. All tests were conducted at 37 °C using a conical needle with inner radius R = 0.410 mm and GelMA/tbPE ink (5/15 wt %).

resulting in smaller-than-expected filament diameters. We also investigated the influence of the printhead speed at a fixed extrusion rate on filament fusion (Figure S19) and determined that higher printhead speed improved printability. Increasing the printhead speed and increasing the print-bed speed are expected to have similar effects on printability; in effect, operating with a higher printhead speed corresponded to operating in the low Q/V region. However, very high printhead speeds (e.g., >5 mm·s^{-1}) led to filament breakage and discontinuous printing. Overall, it can be concluded that, with appropriate optimization of the Q and V ranges to the ink compositions, an excellent deposition performance can be obtained, wherein nearly ideal filaments can be deposited with resolution approaching the nozzle diameters. Filament diameters produced at various Q and V are summarized in Figure S20.

To demonstrate the 3D-printing capabilities of our GelMA/bPE inks, we constructed freestanding porous and nonporous structures that withstood their own weight, as shown in Figure 9. Layered grids were printed to quantify the printing resolution, and the printability index Pr, an often-estimated parameter in printability studies,[72] was calculated. Pr describes the shape resolution by quantifying the susceptibility of square pores to rounding up to a circle after deposition. The printability index is expressed as $Pr = \pi/4C = L^2/16A$ where L is the perimeter of the pore, A is the area of the pore, and the circularity C of the enclosed area is expressed as $C = 4\pi A/L^2$. Because the circularity of a perfect circle is 1 and that of a perfect square is $\pi/4$, Pr becomes a convenient approach for quantifying the pore resolution whereby $Pr = 1$ indicates perfect square pores, $Pr < 1$ indicates more circular pores (undergelation), and $Pr > 1$ is a result of irregular shape (usually resulting from overgelation).[72]

Figure 9A shows representative two-layered 12 × 12 mm grids printed using GelMA/bPE inks at 37 °C where increasing print-bed translational speed V resulted in constructs with higher resolution and well-defined pores. The corresponding dependence of the Pr numbers on V is shown in Figure 9B. While GelMA/dbPE inks were less sensitive to the printhead speed (the Pr values of GelMA/dbPE inks were within the 0.95−1.00 range), GelMA/tbPE inks showed a remarkable improvement in their printability with increasing V, with the Pr number increasing from 0.84 at lower printhead speeds to nearly 1 (perfect square pores) at faster V. Figure S21 shows similar printed structures for other compositions of GelMA/bPE inks. Overall, increasing the bPE content in both GelMA/dbPE and GelMA/tbPE inks resulted in Pr values approaching 1. These minor differences in the printing performance can be attributed to the slightly slower postdeposition recovery of the tbPE inks (Figure 6). Notwithstanding, with subtle optimiza-

https://doi.org/10.1021/acsapm.3c01085
ACS Appl. Polym. Mater. 2024, 6, 2427−2441

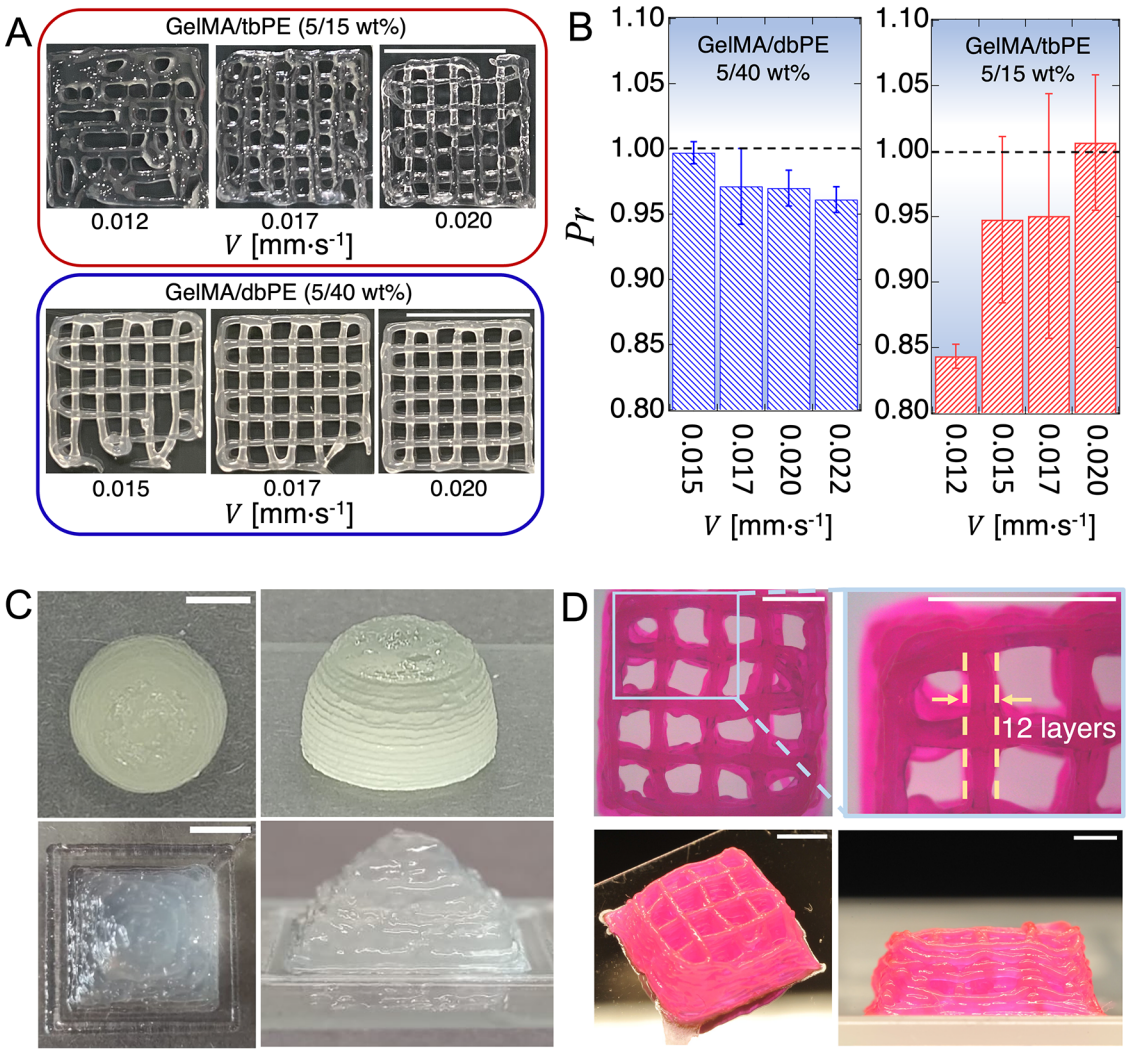

Figure 9. Printability demonstrations of GelMA/bPE inks. (A) Two-layer printing of porous grid structures (scale bar indicates 10 mm) . (B) Estimation of the printability index *Pr* as a function of the translational printhead speed *V*. (C) Freestanding 3D-printed structures (dome and pyramid) constructed using 5/7.5 wt % GelMA/tbPE extruded using a screw-based printer at V = 0.02 mm·s^{-1}. (D) Top and side views of multilayered grid structures with controlled porosity consisting of 12 layers printed using 5/15 wt % GelMA/tbPE and extruded with a pneumatic printer at pressure P = 90 kPa and printhead velocity V = 3 mm·s^{-1}. Scale bars are 4 mm.

tion of the printing conditions, excellent printing performance can be achieved with both dbPE- and tbPE-based inks.

To further exemplify the printing performance of our GelMA/bPE inks, we constructed several 3D shapes, such as porous grids, cubes, pyramids, and domes, with different curvature and height characteristics. Figure 9C highlights the convenient utility of GelMA/bPE inks in building freestanding 3D shapes (dome and pyramid) with minimal optimization. These structures, along with other printed examples, were stable with no time-dependent deformation, as shown in Figure S22. Furthermore, multilayered structures (12-layered grids) printed using a pneumatic printer (Figure 9D) retained their porous structures. When viewed under an optical microscope, the grids maintained well-defined pore sizes and excellent shape fidelity.

CONCLUSIONS

In this paper, we have demonstrated bPE additives that enable 3D printing of gelatin-based inks at physiologically relevant temperatures. The oppositely charged dbPEs or tbPEs self-assemble to form PEC micelles or 3D networks, respectively. When combined with methacrylated gelatin (GelMA), the hierarchical microstructures of the bPE self-assembly were preserved. These assemblies served as a scaffolding for the GelMA chains, providing sufficient viscoelasticity, yielding, and shear-thinning characteristics to the GelMA/bPE inks to enable their high-fidelity printing at 37 °C. In contrast, GelMA solutions, which exhibit a gel−sol transition at temperatures of <30 °C, are unprintable at 37 °C. Moreover, the GelMA/bPE inks recover significantly faster after shearing (at 37 °C) compared GelMA inks (at 22 °C), further contributing to the fidelity of the printed structures upon extrusion and deposition. UV irradiation of GelMA/bPE inks resulted in hydrogels composed of interpenetrating electrostatically cross-linked and covalently cross-linked networks.

The microstructure and the viscoelastic properties of the GelMA/bPE inks and hydrogels were facilely tunable by varying the bPE architecture (di- vs triblock) and concentrations. Moreover, varying the GelMA concentration or DoF of the methacrylate groups enabled further tunability of the viscoelastic properties of the GelMA/bPE inks both before and after photo-cross-linking. By relying on the viscoelastic

https://doi.org/10.1021/acsapm.3c01085
ACS Appl. Polym. Mater. 2024, 6, 2427−2441

properties of the inks, we demonstrate an optimal printing window at 37 °C for the GelMA/bPE inks, within which the extrusion pressure and velocity are tuned to obtain excellent printing performance and fidelity of the printed structures. Taken together with our previous results on the bioperformance of our inks,[46] we envision that our findings will serve as a practical guide for the printing community to formulate highly customizable extrusion-based inks and encourage the adoption of our additive-based approach to other low-viscosity materials to meet the growing demands of suitable inks in 3D-printing applications.

MATERIALS AND METHODS

Materials. Potassium (99.5% trace metals basis), naphthalene, poly(ethylene glycol) (PEG; M_n = 20000 g·mol^{-1}), poly(ethylene glycol) monomethyl ether (mPEG; M_n = 5000 g·mol^{-1}), allyl glycidyl ether (AGE), calcium hydride, sodium 3-mercapto-1-propanesulfonate (technical grade, 90%), 1*H*-pyrazole-1-carboxamidine hydrochloride (99%), cysteamine hydrochloride (≥98%), gelatin (type A, gel strength ∼ 300 g bloom, from porcine skin), methacrylic anhydride, 2,2-dimethoxy-2-phenylacetophenone (DMPA), and Irgacure 2959 were purchased from Sigma-Aldrich. Tetrahydrofuran (THF) and dimethylformamide (DMF) were obtained from Fisher Scientific. Dialysis tubes were received from VWR International and Fisher Scientific. DPBS−/− was purchased from Thermo Fisher Scientific.

Synthesis of GelMA. The synthesis and purification of GelMA were performed as previously described.[36,73] A total of 10 g of gelatin (type A, gel strength ∼ 300 g bloom, from porcine skin, 0.266 mmol of NH_2 groups, 1 equiv) was dissolved in 100 mL of DPBS. The solution was heated to 50 °C until complete dissolution of gelatin. Then, 3.17 mL of methacrylic anhydride (2.13 mmol, 8 equiv per NH_2 group in gelatin) was added dropwise, and the mixture was stirred at 50 °C for 2 h. After dilution with 100 mL of DPBS, the solution was transferred into dialysis tubes [molecular weight cutoff (MWCO) = 12−14 kDa] and dialyzed against deionized water at 40 °C for 12 cycles of 8 h each. After lyophilization, the product was obtained as a white solid and stored at −20 °C. GelMA with different DoFs (low, medium, or high) was obtained by varying the amount of methacrylic anhydride (1, 8, or 20 equiv per NH_2 group in gelatin). ^{1}H NMR (400 MHz, D_2O, 315 K): δ 7.60−7.40 ($H_{aromtic}$, gelatin), 5.88 (1H, H_a, vinyl), 5.64 (1H, H_b, vinyl), 5.24−0.99 (gelatin), 3.20 (bs, 2H, NH_2), 2.11 (s, 3H, CH_3, H_c) (Figure S2).

Synthesis of tbPEs. The synthesis, functionalization, and purification of tbPEs were carried out following previously published protocols (Scheme S2).[48] PEO (20000 g·mol^{-1}) was dried in a vacuum oven at 25 °C for 1 day before use. AGE was mixed with calcium hydride, stirred overnight to remove trace amounts of water, and degassed by three cycles of freeze−pump−thaw, followed by distillation. For copolymer synthesis, all anhydrous reagents were transferred into a glovebox under an argon atmosphere. A total of 30 g of PEO was dissolved in 70 mL of anhydrous THF at 45 °C and titrated with potassium naphthalenide (0.4 M in anhydrous THF) until the solution turned light green. Then, an appropriate amount (∼17 mL) of AGE was added, and the reaction mixture was stirred at 45 °C for 48 h. The anionic polymerization was terminated by adding 10 mL of degassed methanol. After precipitation in hexane, the product was filtered and then dried under vacuum prior to further functionalization. The degree of polymerization (DP) of the PAGE blocks was calculated from the relative peak intensities in the NMR spectra, yielding $PAGE_{30}$−PEO_{455}−$PAGE_{30}$.

For subsequent thiol-ene click functionalization, $PAGE_{30}$−PEO_{455}−$PAGE_{30}$, photoinitiator DMPA, and a functional thiol reagent (cysteamine hydrochloride or sodium 3-mercapto-1-propanesulfonate, 5 equiv per alkene group) were dissolved in a DMF/water (volumetric ratio of 1:1) mixture. After degassing with nitrogen for 30 min, the solutions were irradiated with UV light (365 nm, 8 W) overnight. Then, the product solutions of functionalized copolymers with either ammonium or sulfonate moieties were dialyzed (MWCO = 3.5 kDa) against deionized water for 14 cycles of 8 h each, followed by lyophilization.

Guanidinilated $PAGE_{30}$−PEO_{455}−$PAGE_{30}$ was synthesized from the ammonium-functionalized copolymer. An appropriate amount of the ammonium-functionalized tbPE and 1*H*-pyrazole-1-carboxamidine (4 equiv per ammonium group) was dissolved in 200 mL of a phosphate-buffered saline solution, and the pH was adjusted to 10 with sodium hydroxide. The mixture solution was maintained at pH = 10 and stirred for 3 days at room temperature. Then, the product solution was dialyzed (MWCO = 3.5 kDa) against deionized water for 14 cycles of 8 h each, followed by lyophilization. ^{1}H NMR spectra of triblock copolymers prior to and after functionalization are provided in Figure S3.

Synthesis of dbPEs. The synthesis, functionalization, and purification of dbPEs were performed following the same protocol as that used for tbPEs, except for replacing the initiator PEO with mPEG (5000 g·mol^{-1}). The DP of the PAGE block was calculated from the relative peak intensities in the NMR spectra, yielding $mPEO_{113}$−$PAGE_{45}$. ^{1}H NMR spectra of diblock copolymers prior to and after functionalization are provided in Scheme S1 and Figure S2.

Preparation of GelMA/bPE Inks and Hydrogels. Stock solutions of the block polyanion (sulfonate-functionalized dbPE or tbPE), block polycation (guanidinium-functionalized dbPE or tbPE), GelMA precursor, and photoinitiator Irgacure 2959 were prepared in DBPS. GelMA/dbPE and GelMA/tbPE inks were obtained by mixing the block polyanion with an aqueous solution of GelMA precursor and photoinitiator, followed by the addition of a block polycation. The molar charge ratio of cationic and anionic moieties of ink was set to 1:1. Each addition step was followed by thorough mixing to ensure homogeneity of the samples. Hydrogels were prepared by exposing the inks to UV light (302 nm, 8 W) for photo-cross-linking for 5 min.

SAXS Measurements. SAXS measurements were performed at beamline 12-ID-B at the Advanced Photon Source (APS), Argonne National Laboratory (ANL). The sample-to-detector distance was set to 4 m, corresponding to a wave vector (q) range of 0.0002−0.5 Å^{-1}. bPE and GelMA/bPE inks were loaded into holes (diameter = 3 mm) in 4-mm-thick aluminum strips using a positive-displacement pipet and sealed on both sides with Kapton tape to avoid water evaporation. Photo-cross-linked GelMA/bPE hydrogels were prepared by loading the corresponding inks in the aluminum strips, followed by 5 min of UV exposure, and sealing with Kapton tape. All of the samples were prepared and loaded onto the sample holders at least 24 h before the SAXS measurements. The samples were exposed to 13 keV X-rays for 0.1 s at room temperature. The 2D scattering data were converted into 1D data (I_{sample}) by using the *matSAXS* package. The sample scattering intensity was acquired by subtracting the appropriately scaled background (solvent) scattering intensity ($I_{solvent}$) from the measured scattering intensity, $I(q) = I_{sample} - \alpha I_{solvent}$, with α being the scaling parameter.

Rheology. Shear rheology measurements were performed on an Anton Paar MCR 302 rheometer. A cone-and-plate assembly (diameter = 10 mm; cone angle = 2°) was used for the inks, and a plate−plate geometry (diameter = 8 mm; gap size = 0.6 mm) was used to measure the hydrogels after photo-cross-linking. Appropriate amounts of GelMA/bPE inks were loaded on the lower plate, and excess volume was trimmed once the cone and plate reached the measuring gap. GelMA/bPE hydrogels were prepared by pipetting 75 μL of ink into a cylindrical poly(dimethylsiloxane) mold (diameter = 8 mm; height = 1.5 mm), and the ink was irradiated with UV radiation for 5 min (302 nm, 8 W). The cross-linked GelMA/bPE hydrogels were then transferred to the parallel-plate geometry for measuring. Rheological data were acquired at 37 °C for bPE and GelMA/bPE formulations and hydrogels. A solvent trap and a Peltier temperature control system were used to minimize water evaporation and perform temperature-ramp experiments. Prior to studying the rheological properties, samples were presheared and equilibrated by applying an oscillatory shear γ = 100% for 30 s, followed by γ = 1% for 5 min. This protocol was found to be sufficient for disrupting the microstructure of bPE and GelMA/bPE inks and for tracking their

https://doi.org/10.1021/acsapm.3c01085
ACS Appl. Polym. Mater. 2024, 6, 2427−2441

viscoelastic recovery. The disruption of the microstructure is evident in the amplitude sweeps carried out for all of the inks, where yielding is observed near $\gamma \sim 10\%$ (Figures S8, S10A,B, S16, and S17). We also include representative time sweeps for two PEC inks and two GelMA/PEC inks in Figure S23. As is evident in Figure S23A,B,D,E, both G' and G'' exhibit very low values in the high-strain regime (γ = 100%), which recover to constant moduli in the low-strain regime (γ = 1%). We note that this protocol did not disrupt the covalently cross-linked GelMA networks in the photocured GelMA/bPE hydrogels because the shear moduli did not decrease under the high-amplitude deformations (Figure S23C,F).

3D-Printing Demonstrations. For extrusion-based 3D printing of GelMA/bPE inks, two 3D printers were used. In the first printing setup, the inks were prepared and filled into a 2 mL syringe (Inkjet Luer Lock Solo, VWR) fitted with a conical needle (diameter = 0.25 mm, Vieweg GmbH). The ink-loaded syringe was inserted into a temperature-controlled and piston-driven 3D printer (BioSpot BP, Biofluidix GmbH). In the second printing setup, a BIO X (CELLINK) printer equipped with standard screw-based mechanical and pneumatic air pump printheads was employed. GelMA/bPE inks were loaded into a 3 mL disposable cartridge (CELLINK), which was fitted with a polystyrene standard 22G conical nozzle. In all printing experiments, the temperature was fixed at 37 °C for 30 min before extrusion. Grid structures were printed (12 × 12 mm) using custom-written G-codes and photocured under UV light for 60 s.

■ ASSOCIATED CONTENT

Data Availability Statement

All of the data reported in this paper are available upon request from the corresponding author.

Supporting Information

The Supporting Information is available free of charge at https://pubs.acs.org/doi/10.1021/acsapm.3c01085.

bPE and GelMA synthesis schemes, ^{1}H NMR spectra of precursors, functionalized polymers, and GelMA, oscillatory and rotational shear rheology, scanning electron micrographs of dried and cured hydrogels, SAXS spectra of GelMA, GelMA/dbPE, and GelMA/tbPE inks and hydrogels, filament diameter and spreading ratio from printing fusion tests and as-extruded filaments, printability number Pr as a function of the bPE concentration C_{bPE}, stability of freestanding 3D-printed structures, and determination of the PEC domain arrangements by Bragg peak assignments (PDF)

■ AUTHOR INFORMATION

Corresponding Author

Samanvaya Srivastava − *Chemical and Biomolecular Engineering, University of California, Los Angeles, Los Angeles, California 90095, United States; California NanoSystems Institute and Institute for Carbon Management, University of California, Los Angeles, Los Angeles, California 90095, United States;* orcid.org/0000-0002-3519-7224; Email: samsri@ucla.edu

Authors

Tobias Göckler − *Chemical and Biomolecular Engineering, University of California, Los Angeles, Los Angeles, California 90095, United States; Institute of Functional Interfaces, Karlsruhe Institute of Technology (KIT), 76344 Eggenstein-Leopoldshafen, Germany*

Fahed Albreiki − *Chemical and Biomolecular Engineering, University of California, Los Angeles, Los Angeles, California 90095, United States*

Defu Li − *Chemical and Biomolecular Engineering, University of California, Los Angeles, Los Angeles, California 90095, United States*

Alisa Grimm − *Chemical and Biomolecular Engineering, University of California, Los Angeles, Los Angeles, California 90095, United States; Institute of Functional Interfaces, Karlsruhe Institute of Technology (KIT), 76344 Eggenstein-Leopoldshafen, Germany*

Felix Mecklenburg − *Institute of Functional Interfaces, Karlsruhe Institute of Technology (KIT), 76344 Eggenstein-Leopoldshafen, Germany*

Juan Manuel Urueña − *National Science Foundation (NSF) BioPolymers, Automated Cellular Infrastructure, Flow, and Integrated Chemistry Materials Innovation Platform (BioPACIFIC MIP), University of California, Santa Barbara, Santa Barbara, California 93106, United States*

Ute Schepers − *Institute of Functional Interfaces, Karlsruhe Institute of Technology (KIT), 76344 Eggenstein-Leopoldshafen, Germany; Institute of Organic Chemistry, Karlsruhe Institute of Technology (KIT), 76131 Karlsruhe, Germany*

Complete contact information is available at: https://pubs.acs.org/10.1021/acsapm.3c01085

Author Contributions

†Equal contributions.

Author Contributions

S.S., T.G., and U.S. conceived the study. F.A., T.G., and D.L. performed the synthesis, scattering, and rheology experiments. F.A., A.G., and F.M. performed the 3D-printing studies with help from J.M.U. F.A., T.G., and D.L. analyzed and compiled the results. S.S., U.S., T.G., and F.A. edited the manuscript with input from D.L. and A.G.

Notes

The authors declare no competing financial interest.

■ ACKNOWLEDGMENTS

Research at University of California, Los Angeles, was supported by the NSF via the CAREER program (DMR-2048285). Research at the KIT was funded by the Deutsche Forschungsgemeinschaft (German Research Foundation) under Germany's Excellence Strategy via the Excellence Cluster 3D Matter Made to Order (EXC-2082/1-390761711). This research used resources of the APS, a U.S. Department of Energy (DOE), Office of Science User Facility, operated for the DOE Office of Science by ANL under Contract DE-AC02-06CH11357. F.A., J.M.U., and S.S. thank Prof. Angela Pitenis for assistance in imaging the printed manifolds. T.G. acknowledges support from the Helmholtz Program Information: Materials Systems Engineering. F.A. acknowledges funding support of the United Arab Emirates University under the national teaching assistant program. A.G. acknowledges funding support by the Karlsruhe House of Young Scientists. Part of this work was supported by the NSF BioPACIFIC MIP under Award DMR-1933487.

■ REFERENCES

(1) García-Alvarado, R.; Moroni-Orellana, G.; Banda-Pérez, P. Architectural Evaluation of 3D-Printed Buildings. *Buildings* **2021**, *11* (6), 254.

(2) Sakin, M.; Kiroglu, Y. C. 3D Printing of Buildings: Construction of the Sustainable Houses of the Future by BIM. *Energy Procedia* **2017**, *134*, 702−711.
(3) Nickels, L. AM and aerospace: an ideal combination. *Metal Powder Report* **2015**, *70* (6), 300−303.
(4) Kumar, L. J.; Krishnadas Nair, C. Current trends of additive manufacturing in the aerospace industry. In *Advances in 3D Printing & Additive Manufacturing Technologies*; Wimpenny, D.; Pandey, P.; Kumar, L., Eds.; Springer, 2017; pp 39−54
(5) Nichols, M. R. How does the automotive industry benefit from 3D metal printing? *Metal Powder Report* **2019**, *74* (5), 257−258.
(6) Böckin, D.; Tillman, A.-M. Environmental assessment of additive manufacturing in the automotive industry. *Journal of Cleaner Production* **2019**, *226*, 977−987.
(7) Halassi, S.; Semeijn, J.; Kiratli, N. From consumer to prosumer: a supply chain revolution in 3D printing. *International Journal of Physical Distribution & Logistics Management* **2019**, *49* (2), 200−216.
(8) Yoo, B.; Ko, H.; Chun, S. Prosumption perspectives on additive manufacturing: reconfiguration of consumer products with 3D printing. *Rapid Prototyping Journal* **2016**, *22* (4), 691−705.
(9) Gebler, M.; Schoot Uiterkamp, A. J. M.; Visser, C. A global sustainability perspective on 3D printing technologies. *Energy Policy* **2014**, *74*, 158−167.
(10) Ozbolat, I. T.; Peng, W.; Ozbolat, V. Application areas of 3D bioprinting. *Drug Discovery Today* **2016**, *21* (8), 1257−1271.
(11) Ozbolat, I. T.; Yu, Y. Bioprinting Toward Organ Fabrication: Challenges and Future Trends. *IEEE Trans. Biomed. Eng.* **2013**, *60* (3), 691−699.
(12) Mironov, V.; Kasyanov, V.; Drake, C.; Markwald, R. R. Organ printing: promises and challenges. *Regenerative Medicine* **2008**, *3* (1), 93−103.
(13) Kolesky, D. B.; Truby, R. L.; Gladman, A. S.; Busbee, T. A.; Homan, K. A.; Lewis, J. A. 3D bioprinting of vascularized, heterogeneous cell-laden tissue constructs. *Adv. Mater.* **2014**, *26* (19), 3124−3130.
(14) Hospodiuk, M.; Dey, M.; Sosnoski, D.; Ozbolat, I. T. The bioink: A comprehensive review on bioprintable materials. *Biotechnol. Adv.* **2017**, *35* (2), 217−239.
(15) Gungor-Ozkerim, P. S.; Inci, I.; Zhang, Y. S.; Khademhosseini, A.; Dokmeci, M. R. Bioinks for 3D bioprinting: an overview. *Biomaterials Science* **2018**, *6* (5), 915−946.
(16) Bishop, E. S.; Mostafa, S.; Pakvasa, M.; Luu, H. H.; Lee, M. J.; Wolf, J. M.; Ameer, G. A.; He, T.-C.; Reid, R. R. 3-D bioprinting technologies in tissue engineering and regenerative medicine: Current and future trends. *Genes & Diseases* **2017**, *4* (4), 185−195.
(17) Valot, L.; Martinez, J.; Mehdi, A.; Subra, G. Chemical insights into bioinks for 3D printing. *Chem. Soc. Rev.* **2019**, *48* (15), 4049−4086.
(18) Moroni, L.; Burdick, J. A.; Highley, C.; Lee, S. J.; Morimoto, Y.; Takeuchi, S.; Yoo, J. J. Biofabrication strategies for 3D in vitro models and regenerative medicine. *Nature Reviews Materials* **2018**, *3* (5), 21−37.
(19) Sun, W.; Starly, B.; Daly, A. C.; Burdick, J. A.; Groll, J.; Skeldon, G.; Shu, W.; Sakai, Y.; Shinohara, M.; Nishikawa, M.; Jang, J.; Cho, D.-W.; Nie, M.; Takeuchi, S.; Ostrovidov, S.; Khademhosseini, A.; Kamm, R. D.; Mironov, V.; Moroni, L.; Ozbolat, I. T. The bioprinting roadmap. *Biofabrication* **2020**, *12* (2), No. 022002.
(20) Murphy, S. V.; Atala, A. 3D bioprinting of tissues and organs. *Nat. Biotechnol.* **2014**, *32* (8), 773−785.
(21) Arslan-Yildiz, A.; Assal, R. E.; Chen, P.; Guven, S.; Inci, F.; Demirci, U. Towards artificial tissue models: past, present, and future of 3D bioprinting. *Biofabrication* **2016**, *8* (1), No. 014103.
(22) Bedell, M. L.; Navara, A. M.; Du, Y.; Zhang, S.; Mikos, A. G. Polymeric Systems for Bioprinting. *Chem. Rev.* **2020**, *120* (19), 10744−10792.
(23) Ozbolat, I. T.; Hospodiuk, M. Current advances and future perspectives in extrusion-based bioprinting. *Biomaterials* **2016**, *76*, 321−343.
(24) Malda, J.; Visser, J.; Melchels, F. P.; Jüngst, T.; Hennink, W. E.; Dhert, W. J.; Groll, J.; Hutmacher, D. W. 25th anniversary article: engineering hydrogels for biofabrication. *Adv. Mater.* **2013**, *25* (36), 5011−5028.
(25) Levato, R.; Jungst, T.; Scheuring, R. G.; Blunk, T.; Groll, J.; Malda, J. From shape to function: the next step in bioprinting. *Adv. Mater.* **2020**, *32* (12), No. 1906423.
(26) Ouyang, L. Pushing the rheological and mechanical boundaries of extrusion-based 3D bioprinting. *Trends Biotechnol.* **2022**, *40* (7), 891−902.
(27) Paxton, N.; Smolan, W.; Böck, T.; Melchels, F.; Groll, J.; Jungst, T. Proposal to assess printability of bioinks for extrusion-based bioprinting and evaluation of rheological properties governing bioprintability. *Biofabrication* **2017**, *9* (4), No. 044107.
(28) Lee, S. C.; Gillispie, G.; Prim, P.; Lee, S. J. Physical and Chemical Factors Influencing the Printability of Hydrogel-based Extrusion Bioinks. *Chem. Rev.* **2020**, *120* (19), 10834−10886.
(29) Blaeser, A.; Duarte Campos, D. F.; Puster, U.; Richtering, W.; Stevens, M. M.; Fischer, H. Controlling shear stress in 3D bioprinting is a key factor to balance printing resolution and stem cell integrity. *Adv. Healthcare Mater.* **2016**, *5* (3), 326−333.
(30) Townsend, J. M.; Beck, E. C.; Gehrke, S. H.; Berkland, C. J.; Detamore, M. S. Flow behavior prior to crosslinking: The need for precursor rheology for placement of hydrogels in medical applications and for 3D bioprinting. *Prog. Polym. Sci.* **2019**, *91*, 126−140.
(31) Xie, M.; Yu, K.; Sun, Y.; Shao, L.; Nie, J.; Gao, Q.; Qiu, J.; Fu, J.; Chen, Z.; He, Y. Protocols of 3D bioprinting of gelatin methacryloyl hydrogel based bioinks. *JoVE (Journal of Visualized Experiments)* **2019**, *154*, No. e60545.
(32) Nichol, J. W.; Koshy, S. T.; Bae, H.; Hwang, C. M.; Yamanlar, S.; Khademhosseini, A. Cell-laden microengineered gelatin methacrylate hydrogels. *Biomaterials* **2010**, *31* (21), 5536−5544.
(33) Gaudet, I. D.; Shreiber, D. I. Characterization of Methacrylated Type-I Collagen as a Dynamic, Photoactive Hydrogel. *Biointerphases* **2012**, *7* (1), No. 25.
(34) Liu, W.; Heinrich, M. A.; Zhou, Y.; Akpek, A.; Hu, N.; Liu, X.; Guan, X.; Zhong, Z.; Jin, X.; Khademhosseini, A.; Zhang, Y. S. Extrusion bioprinting of shear-thinning gelatin methacryloyl bioinks. *Adv. Healthcare Mater.* **2017**, *6* (12), No. 1601451.
(35) Klotz, B. J.; Gawlitta, D.; Rosenberg, A. J. W. P.; Malda, J.; Melchels, F. P. W. Gelatin-Methacryloyl Hydrogels: Towards Biofabrication-Based Tissue Repair. *Trends Biotechnol.* **2016**, *34* (5), 394−407.
(36) Yue, K.; Trujillo-de Santiago, G.; Alvarez, M. M.; Tamayol, A.; Annabi, N.; Khademhosseini, A. Synthesis, properties, and biomedical applications of gelatin methacryloyl (GelMA) hydrogels. *Biomaterials* **2015**, *73*, 254−271.
(37) Janmaleki, M.; Liu, J.; Kamkar, M.; Azarmanesh, M.; Sundararaj, U.; Nezhad, A. S. Role of temperature on bio-printability of gelatin methacryloyl bioink in two-step cross-linking strategy for tissue engineering applications. *Biomedical Materials* **2021**, *16* (1), No. 015021.
(38) Burdick, J. A.; Chung, C.; Jia, X.; Randolph, M. A.; Langer, R. Controlled Degradation and Mechanical Behavior of Photopolymerized Hyaluronic Acid Networks. *Biomacromolecules* **2005**, *6* (1), 386−391.
(39) Pati, F.; Jang, J.; Lee, J. W.; Cho, D.-W. Extrusion Bioprinting. In *Essentials of 3D Biofabrication and Translation*; Atala, A., Yoo, J. J., Eds.; Academic Press, 2015; Chapter 7, pp 123−152, https://doi.org/10.1016/B978-0-12-800972-7.00007-4.
(40) Ashammakhi, N.; Ahadian, S.; Xu, C.; Montazerian, H.; Ko, H.; Nasiri, R.; Barros, N.; Khademhosseini, A. Bioinks and bioprinting technologies to make heterogeneous and biomimetic tissue constructs. *Materials Today Bio* **2019**, *1*, No. 100008.
(41) Hölzl, K.; Lin, S.; Tytgat, L.; Van Vlierberghe, S.; Gu, L.; Ovsianikov, A. Bioink properties before, during and after 3D bioprinting. *Biofabrication* **2016**, *8* (3), No. 032002.
(42) Gao, G.; Schilling, A. F.; Hubbell, K.; Yonezawa, T.; Truong, D.; Hong, Y.; Dai, G.; Cui, X. Improved properties of bone and

cartilage tissue from 3D inkjet-bioprinted human mesenchymal stem cells by simultaneous deposition and photocrosslinking in PEG-GelMA. *Biotechnol. Lett.* **2015**, *37*, 2349−2355.
(43) Hutson, C. B.; Nichol, J. W.; Aubin, H.; Bae, H.; Yamanlar, S.; Al-Haque, S.; Koshy, S. T.; Khademhosseini, A. Synthesis and characterization of tunable poly (ethylene glycol): gelatin methacrylate composite hydrogels. *Tissue Engineering Part A* **2011**, *17* (13−14), 1713−1723.
(44) Kim, P.; Yuan, A.; Nam, K.-H.; Jiao, A.; Kim, D.-H. Fabrication of poly (ethylene glycol): gelatin methacrylate composite nanostructures with tunable stiffness and degradation for vascular tissue engineering. *Biofabrication* **2014**, *6* (2), No. 024112.
(45) Nemeth, C. L.; Janebodin, K.; Yuan, A. E.; Dennis, J. E.; Reyes, M.; Kim, D.-H. Enhanced chondrogenic differentiation of dental pulp stem cells using nanopatterned PEG-GelMA-HA hydrogels. *Tissue Engineering Part A* **2014**, *20* (21−22), 2817−2829.
(46) Gockler, T.; Li, D.; Grimm, A.; Mecklenburg, F.; Grün, M.; Schepers, U.; Srivastava, S. Polyelectrolyte Complex Hydrogel Scaffoldings Enable Extrusion-based 3D Bioprinting of Low-Viscosity Bioinks. *ChemRxiv* **2023**, DOI: 10.26434/chemrxiv-2023-v2tx2-v2.
(47) Li, D.; Göckler, T.; Schepers, U.; Srivastava, S. Polyelectrolyte Complex-Covalent Interpenetrating Polymer Network Hydrogels. *Macromolecules* **2022**, *55* (11), 4481−4491.
(48) Hunt, J. N.; Feldman, K. E.; Lynd, N. A.; Deek, J.; Campos, L. M.; Spruell, J. M.; Hernandez, B. M.; Kramer, E. J.; Hawker, C. J. Tunable, high modulus hydrogels driven by ionic coacervation. *Adv. Mater.* **2011**, *23* (20), 2327−2331.
(49) Srivastava, S.; Levi, A. E.; Goldfeld, D. J.; Tirrell, M. V. Structure, morphology, and rheology of polyelectrolyte complex hydrogels formed by self-assembly of oppositely charged triblock polyelectrolytes. *Macromolecules* **2020**, *53* (14), 5763−5774.
(50) Srivastava, S.; Andreev, M.; Levi, A. E.; Goldfeld, D. J.; Mao, J.; Heller, W. T.; Prabhu, V. M.; De Pablo, J. J.; Tirrell, M. V. Gel phase formation in dilute triblock copolyelectrolyte complexes. *Nat. Commun.* **2017**, *8*, No. 14131.
(51) Lemmers, M.; Voets, I. K.; Cohen Stuart, M. A.; van der Gucht, J. Transient network topology of interconnected polyelectrolyte complex micelles. *Soft Matter* **2011**, *7* (4), 1378−1389.
(52) Li, D.; Ghovvati, M.; Annabi, N.; Srivastava, S. Polyelectrolyte Complex Scaffoldings for Photocrosslinked Hydrogels. *Molecular Systems Design & Engineering* **2023**, *8*, 611−623.
(53) Bertassoni, L. E.; Cardoso, J. C.; Manoharan, V.; Cristino, A. L.; Bhise, N. S.; Araujo, W. A.; Zorlutuna, P.; Vrana, N. E.; Ghaemmaghami, A. M.; Dokmeci, M. R.; Khademhosseini, A. Direct-write bioprinting of cell-laden methacrylated gelatin hydrogels. *Biofabrication* **2014**, *6* (2), No. 024105.
(54) Van Den Bulcke, A. I.; Bogdanov, B.; De Rooze, N.; Schacht, E. H.; Cornelissen, M.; Berghmans, H. Structural and rheological properties of methacrylamide modified gelatin hydrogels. *Biomacromolecules* **2000**, *1* (1), 31−38.
(55) Gao, G.; Schilling, A. F.; Hubbell, K.; Yonezawa, T.; Truong, D.; Hong, Y.; Dai, G.; Cui, X. Improved properties of bone and cartilage tissue from 3D inkjet-bioprinted human mesenchymal stem cells by simultaneous deposition and photocrosslinking in PEG-GelMA. *Biotechnol. Lett.* **2015**, *37* (11), 2349−2355.
(56) Yue, Y.; Gong, J. P. Structure and Unique Functions of Anisotropic Hydrogels Comprising Uniaxially Aligned Lamellar Bilayers. *Bull. Chem. Soc. Jpn.* **2021**, *94* (9), 2221−2234.
(57) Swain, P.; Ronghe, A.; Bhutani, U.; Majumdar, S. Physicochemical Response of Gelatin in a Coulombic Soup of Monovalent Salt: A Molecular Simulation and Experimental Study. *J. Phys. Chem. B* **2019**, *123* (5), 1186−1194.
(58) Ben Messaoud, G.; Aveic, S.; Wachendoerfer, M.; Fischer, H.; Richtering, W. 3D Printable Gelatin Methacryloyl (GelMA)-Dextran Aqueous Two-Phase System with Tunable Pores Structure and Size Enables Physiological Behavior of Embedded Cells In Vitro. *Small* **2023**, *19*, No. 2208089.
(59) Safaei-Yaraziz, A.; Akbari-Birgani, S.; Nikfarjam, N. Porous scaffolds with the structure of an interpenetrating polymer network made by gelatin methacrylated nanoparticle-stabilized high internal phase emulsion polymerization targeted for tissue engineering. *RSC Adv.* **2021**, *11* (37), 22544−22555.
(60) Bohidar, H. B. Hydrodynamic properties of gelatin in dilute solutions. *Int. J. Biol. Macromol.* **1998**, *23* (1), 1−6.
(61) Cooke, M. E.; Rosenzweig, D. H. The rheology of direct and suspended extrusion bioprinting. *APL Bioengineering* **2021**, *5* (1), No. 011502.
(62) Lopez Hernandez, H.; Souza, J. W.; Appel, E. A. A Quantitative Description for Designing the Extrudability of Shear-Thinning Physical Hydrogels. *Macromol. Biosci.* **2021**, *21* (2), No. 2000295.
(63) Coussot, P. Yield stress fluid flows: A review of experimental data. *J. Non-Newtonian Fluid Mech.* **2014**, *211*, 31−49.
(64) Krogstad, D. V.; Lynd, N. A.; Choi, S.-H.; Spruell, J. M.; Hawker, C. J.; Kramer, E. J.; Tirrell, M. V. Effects of Polymer and Salt Concentration on the Structure and Properties of Triblock Copolymer Coacervate Hydrogels. *Macromolecules* **2013**, *46* (4), 1512−1518.
(65) Kim, J.-M.; Heo, T.-Y.; Choi, S.-H. Structure and Relaxation Dynamics for Complex Coacervate Hydrogels Formed by ABA Triblock Copolymers. *Macromolecules* **2020**, *53* (21), 9234−9243.
(66) Yasuda, K.; Armstrong, R.; Cohen, R. Shear flow properties of concentrated solutions of linear and star branched polystyrenes. *Rheol. Acta* **1981**, *20* (2), 163−178.
(67) Jungst, T.; Smolan, W.; Schacht, K.; Scheibel, T.; Groll, J. r. Strategies and molecular design criteria for 3D printable hydrogels. *Chem. Rev.* **2016**, *116* (3), 1496−1539.
(68) Cox, W.; Merz, E. Correlation of dynamic and steady flow viscosities. *J. Polym. Sci.* **1958**, *28* (118), 619−622.
(69) Annable, T.; Buscall, R.; Ettelaie, R.; Whittlestone, D. The rheology of solutions of associating polymers: Comparison of experimental behavior with transient network theory. *J. Rheol.* **1993**, *37* (4), 695−726.
(70) Mewis, J.; Wagner, N. J. Thixotropy. *Adv. Colloid Interface Sci.* **2009**, *147-148*, 214−227.
(71) Ahmadi Soufivand, A.; Faber, J.; Hinrichsen, J.; Budday, S. Multilayer 3D bioprinting and complex mechanical properties of alginate-gelatin mesostructures. *Sci. Rep.* **2023**, *13* (1), No. 11253.
(72) Ouyang, L.; Yao, R.; Zhao, Y.; Sun, W. Effect of bioink properties on printability and cell viability for 3D bioplotting of embryonic stem cells. *Biofabrication* **2016**, *8* (3), No. 035020.
(73) Göckler, T.; Haase, S.; Kempter, X.; Pfister, R.; Maciel, B. R.; Grimm, A.; Molitor, T.; Willenbacher, N.; Schepers, U. Tuning Superfast Curing Thiol-Norbornene-Functionalized Gelatin Hydrogels for 3D Bioprinting. *Adv. Healthcare Mater.* **2021**, *10* (14), No. 2100206.